

MIT Open Access Articles

Measurement of the $\gamma\gamma^ \rightarrow n$ and $\gamma\gamma^* \rightarrow n\pi$ transition form factors*

The MIT Faculty has made this article openly available. **Please share** how this access benefits you. Your story matters.

Citation: del Amo Sanchez, P. et al. "Measurement of the $\gamma\gamma^* \rightarrow n$ and $\gamma\gamma^* \rightarrow n\pi$ transition form factors." Physical Review D 84, 052001 (2011) [19 pages]. © 2011 American Physical Society.

As Published: <http://dx.doi.org/10.1103/PhysRevD.84.052001>

Publisher: American Physical Society

Persistent URL: <http://hdl.handle.net/1721.1/69854>

Version: Final published version: final published article, as it appeared in a journal, conference proceedings, or other formally published context

Terms of Use: Article is made available in accordance with the publisher's policy and may be subject to US copyright law. Please refer to the publisher's site for terms of use.



Measurement of the $\gamma\gamma^* \rightarrow \eta$ and $\gamma\gamma^* \rightarrow \eta'$ transition form factors

P. del Amo Sanchez,¹ J. P. Lees,¹ V. Poireau,¹ E. Prencipe,¹ V. Tisserand,¹ J. Garra Tico,² E. Grauges,² M. Martinelli,^{3a,3b}
D. A. Milanese,^{3a} A. Palano,^{3a,3b} M. Pappagallo,^{3a,3b} G. Eigen,⁴ B. Stugu,⁴ L. Sun,⁴ D. N. Brown,⁵ L. T. Kerth,⁵
Yu. G. Kolomensky,⁵ G. Lynch,⁵ I. L. Osipenkov,⁵ H. Koch,⁶ T. Schroeder,⁶ D. J. Asgeirsson,⁷ C. Hearty,⁷ T. S. Mattison,⁷
J. A. McKenna,⁷ A. Khan,⁸ V. E. Blinov,⁹ A. A. Botov,⁹ A. R. Buzykaev,⁹ V. P. Druzhinin,⁹ V. B. Golubev,⁹
E. A. Kravchenko,⁹ A. P. Onuchin,⁹ S. I. Serebnyakov,⁹ Yu. I. Skovpen,⁹ E. P. Solodov,⁹ K. Yu. Todyshev,⁹ A. N. Yushkov,⁹
M. Bondioli,¹⁰ S. Curry,¹⁰ D. Kirkby,¹⁰ A. J. Lankford,¹⁰ M. Mandelkern,¹⁰ E. C. Martin,¹⁰ D. P. Stoker,¹⁰ H. Atmacan,¹¹
J. W. Gary,¹¹ F. Liu,¹¹ O. Long,¹¹ G. M. Vitug,¹¹ C. Campagnari,¹² T. M. Hong,¹² D. Kovalskyi,¹² J. D. Richman,¹²
C. A. West,¹² A. M. Eisner,¹³ C. A. Heusch,¹³ J. Kroseberg,¹³ W. S. Lockman,¹³ A. J. Martinez,¹³ T. Schalk,¹³
B. A. Schumm,¹³ A. Seiden,¹³ L. O. Winstrom,¹³ C. H. Cheng,¹⁴ D. A. Doll,¹⁴ B. Echenard,¹⁴ D. G. Hitlin,¹⁴
P. Ongmongkolkul,¹⁴ F. C. Porter,¹⁴ A. Y. Rakitin,¹⁴ R. Andreassen,¹⁵ M. S. Dubrovin,¹⁵ B. T. Meadows,¹⁵
M. D. Sokoloff,¹⁵ P. C. Bloom,¹⁶ W. T. Ford,¹⁶ A. Gaz,¹⁶ M. Nagel,¹⁶ U. Nauenberg,¹⁶ J. G. Smith,¹⁶ S. R. Wagner,¹⁶
R. Ayad,^{17,*} W. H. Toki,¹⁷ H. Jasper,¹⁸ A. Petzold,¹⁸ B. Spaan,¹⁸ M. J. Kobel,¹⁹ K. R. Schubert,¹⁹ R. Schwierz,¹⁹
D. Bernard,²⁰ M. Verderi,²⁰ P. J. Clark,²¹ S. Playfer,²¹ J. E. Watson,²¹ M. Andreotti,^{22a,22b} D. Bettoni,^{22a} C. Bozzi,^{22a}
R. Calabrese,^{22a,22b} A. Cecchi,^{22a,22b} G. Cibinetto,^{22a,22b} E. Fioravanti,^{22a,22b} P. Franchini,^{22a,22b} I. Garzia,^{22a,22b}
E. Luppi,^{22a,22b} M. Munerato,^{22a,22b} M. Negrini,^{22a,22b} A. Petrella,^{22a,22b} L. Piemontese,^{22a} R. Baldini-Ferroli,²³
A. Calcaterra,²³ R. de Sangro,²³ G. Finocchiaro,²³ M. Nicolaci,²³ S. Pacetti,²³ P. Patteri,²³ I. M. Peruzzi,^{23,†} M. Piccolo,²³
M. Rama,²³ A. Zallo,²³ R. Contri,^{24a,24b} E. Guido,^{24a,24b} M. Lo Vetere,^{24a,24b} M. R. Monge,^{24a,24b} S. Passaggio,^{24a}
C. Patrignani,^{24a,24b} E. Robutti,^{24a} B. Bhuyan,²⁵ V. Prasad,²⁵ C. L. Lee,²⁶ M. Morii,²⁶ A. J. Edwards,²⁷ A. Adametz,²⁸
J. Marks,²⁸ U. Uwer,²⁸ F. U. Bernlochner,²⁹ M. Ebert,²⁹ H. M. Lacker,²⁹ T. Lueck,²⁹ A. Volk,²⁹ P. D. Dauncey,³⁰
M. Tibbetts,³⁰ P. K. Behera,³¹ U. Mallik,³¹ C. Chen,³² J. Cochran,³² H. B. Crawley,³² W. T. Meyer,³² S. Prell,³²
E. I. Rosenberg,³² A. E. Rubin,³² A. V. Gritsan,³³ Z. J. Guo,³³ N. Arnaud,³⁴ M. Davier,³⁴ D. Derkach,³⁴
J. Firmino da Costa,³⁴ G. Grosdidier,³⁴ F. Le Diberder,³⁴ A. M. Lutz,³⁴ B. Malaescu,³⁴ A. Perez,³⁴ P. Roudeau,³⁴
M. H. Schune,³⁴ J. Serrano,³⁴ V. Sordini,^{34,‡} A. Stocchi,³⁴ L. Wang,³⁴ G. Wormser,³⁴ D. J. Lange,³⁵ D. M. Wright,³⁵
I. Bingham,³⁶ C. A. Chavez,³⁶ J. P. Coleman,³⁶ J. R. Fry,³⁶ E. Gabathuler,³⁶ D. E. Hutchcroft,³⁶ D. J. Payne,³⁶
C. Touramanis,³⁶ A. J. Bevan,³⁷ F. Di Lodovico,³⁷ R. Sacco,³⁷ M. Sigamani,³⁷ G. Cowan,³⁸ S. Paramesvaran,³⁸
A. C. Wren,³⁸ D. N. Brown,³⁹ C. L. Davis,³⁹ A. G. Denig,⁴⁰ M. Fritsch,⁴⁰ W. Gradl,⁴⁰ A. Hafner,⁴⁰ K. E. Alwyn,⁴¹
D. Bailey,⁴¹ R. J. Barlow,⁴¹ G. Jackson,⁴¹ G. D. Lafferty,⁴¹ J. Anderson,⁴² R. Cenci,⁴² A. Jawahery,⁴² D. A. Roberts,⁴²
G. Simi,⁴² J. M. Tuggle,⁴² C. Dallapiccola,⁴³ E. Salvati,⁴³ R. Cowan,⁴⁴ D. Dujmic,⁴⁴ G. Sciolla,⁴⁴ M. Zhao,⁴⁴
D. Lindemann,⁴⁵ P. M. Patel,⁴⁵ S. H. Robertson,⁴⁵ M. Schram,⁴⁵ P. Biassoni,^{46a,46b} A. Lazzaro,^{46a,46b} V. Lombardo,^{46a}
F. Palombo,^{46a,46b} S. Stracka,^{46a,46b} L. Cremaldi,⁴⁷ R. Godang,^{47,§} R. Kroeger,⁴⁷ P. Sonnek,⁴⁷ D. J. Summers,⁴⁷
X. Nguyen,⁴⁸ M. Simard,⁴⁸ P. Taras,⁴⁸ G. De Nardo,^{49a,49b} D. Monorchio,^{49a,49b} G. Onorato,^{49a,49b} C. Sciacca,^{49a,49b}
G. Raven,⁵⁰ H. L. Snoek,⁵⁰ C. P. Jessop,⁵¹ K. J. Knoepfel,⁵¹ J. M. LoSecco,⁵¹ W. F. Wang,⁵¹ L. A. Corwin,⁵²
K. Honscheid,⁵² R. Kass,⁵² N. L. Blount,⁵³ J. Brau,⁵³ R. Frey,⁵³ O. Igonkina,⁵³ J. A. Kolb,⁵³ R. Rahmat,⁵³ N. B. Sinev,⁵³
D. Strom,⁵³ J. Strube,⁵³ E. Torrence,⁵³ G. Castelli,^{54a,54b} E. Feltresi,^{54a,54b} N. Gagliardi,^{54a,54b} M. Margoni,^{54a,54b}
M. Morandin,^{54a} M. Posocco,^{54a} M. Rotondo,^{54a} F. Simonetto,^{54a,54b} R. Stroili,^{54a,54b} E. Ben-Haim,⁵⁵ M. Bomben,⁵⁵
G. R. Bonneaud,⁵⁵ H. Briand,⁵⁵ G. Calderini,⁵⁵ J. Chauveau,⁵⁵ O. Hamon,⁵⁵ Ph. Leruste,⁵⁵ G. Marchiori,⁵⁵ J. Ocariz,⁵⁵
J. Prendki,⁵⁵ S. Sitt,⁵⁵ M. Biasini,^{56a,56b} E. Manoni,^{56a,56b} A. Rossi,^{56a,56b} C. Angelini,^{57a,57b} G. Batignani,^{57a,57b}
S. Bettarini,^{57a,57b} M. Carpinelli,^{57a,57b,||} G. Casarosa,^{57a,57b} A. Cervelli,^{57a,57b} F. Forti,^{57a,57b} M. A. Giorgi,^{57a,57b}
A. Lusiani,^{57a,57c} N. Neri,^{57a,57b} E. Paoloni,^{57a,57b} G. Rizzo,^{57a,57b} J. J. Walsh,^{57a} D. Lopes Pegna,⁵⁸ C. Lu,⁵⁸ J. Olsen,⁵⁸
A. J. S. Smith,⁵⁸ A. V. Telnov,⁵⁸ F. Anulli,^{59a} E. Baracchini,^{59a,59b} G. Cavoto,^{59a} R. Faccini,^{59a,59b} F. Ferrarotto,^{59a}
F. Ferroni,^{59a,59b} M. Gaspero,^{59a,59b} L. Li Gioi,^{59a} M. A. Mazzoni,^{59a} G. Piredda,^{59a} F. Renga,^{59a,59b} C. Buenger,⁶⁰
T. Hartmann,⁶⁰ T. Leddig,⁶⁰ H. Schröder,⁶⁰ R. Waldi,⁶⁰ T. Adye,⁶¹ E. O. Olaiya,⁶¹ F. F. Wilson,⁶¹ S. Emery,⁶²
G. Hamel de Monchenault,⁶² G. Vasseur,⁶² Ch. Yèche,⁶² M. T. Allen,⁶³ D. Aston,⁶³ D. J. Bard,⁶³ R. Bartoldus,⁶³
J. F. Benitez,⁶³ C. Cartaro,⁶³ M. R. Convery,⁶³ J. Dorfan,⁶³ G. P. Dubois-Felsmann,⁶³ W. Dunwoodie,⁶³ R. C. Field,⁶³
M. Franco Sevilla,⁶³ B. G. Fulsom,⁶³ A. M. Gabareen,⁶³ M. T. Graham,⁶³ P. Grenier,⁶³ C. Hast,⁶³ W. R. Innes,⁶³
M. H. Kelsey,⁶³ H. Kim,⁶³ P. Kim,⁶³ M. L. Kocian,⁶³ D. W. G. S. Leith,⁶³ P. Lewis,⁶³ S. Li,⁶³ B. Lindquist,⁶³ S. Luitz,⁶³
V. Luth,⁶³ H. L. Lynch,⁶³ D. B. MacFarlane,⁶³ D. R. Muller,⁶³ H. Neal,⁶³ S. Nelson,⁶³ C. P. O'Grady,⁶³ I. Ofte,⁶³ M. Perl,⁶³
T. Pulliam,⁶³ B. N. Ratcliff,⁶³ A. Roodman,⁶³ A. A. Salnikov,⁶³ V. Santoro,⁶³ R. H. Schindler,⁶³ J. Schwiening,⁶³
A. Snyder,⁶³ D. Su,⁶³ M. K. Sullivan,⁶³ S. Sun,⁶³ K. Suzuki,⁶³ J. M. Thompson,⁶³ J. Va'vra,⁶³ A. P. Wagner,⁶³ M. Weaver,⁶³

W. J. Wisniewski,⁶³ M. Wittgen,⁶³ D. H. Wright,⁶³ H. W. Wulsin,⁶³ A. K. Yarritu,⁶³ C. C. Young,⁶³ V. Ziegler,⁶³ X. R. Chen,⁶⁴ W. Park,⁶⁴ M. V. Purohit,⁶⁴ R. M. White,⁶⁴ J. R. Wilson,⁶⁴ A. Randle-Conde,⁶⁵ S. J. Sekula,⁶⁵ M. Bellis,⁶⁶ P. R. Burchat,⁶⁶ T. S. Miyashita,⁶⁶ S. Ahmed,⁶⁷ M. S. Alam,⁶⁷ J. A. Ernst,⁶⁷ B. Pan,⁶⁷ M. A. Saeed,⁶⁷ S. B. Zain,⁶⁷ N. Guttman,⁶⁸ A. Soffer,⁶⁸ P. Lund,⁶⁹ S. M. Spanier,⁶⁹ R. Eckmann,⁷⁰ J. L. Ritchie,⁷⁰ A. M. Ruland,⁷⁰ C. J. Schilling,⁷⁰ R. F. Schwitters,⁷⁰ B. C. Wray,⁷⁰ J. M. Izen,⁷¹ X. C. Lou,⁷¹ F. Bianchi,^{72a,72b} D. Gamba,^{72a,72b} M. Pelliccioni,^{72a,72b} L. Lanceri,^{73a,73b} L. Vitale,^{73a,73b} N. Lopez-March,⁷⁴ F. Martinez-Vidal,⁷⁴ A. Oyanguren,⁷⁴ H. Ahmed,⁷⁵ J. Albert,⁷⁵ Sw. Banerjee,⁷⁵ H. H. F. Choi,⁷⁵ K. Hamano,⁷⁵ G. J. King,⁷⁵ R. Kowalewski,⁷⁵ M. J. Lewczuk,⁷⁵ C. Lindsay,⁷⁵ I. M. Nugent,⁷⁵ J. M. Roney,⁷⁵ R. J. Sobie,⁷⁵ T. J. Gershon,⁷⁶ P. F. Harrison,⁷⁶ T. E. Latham,⁷⁶ E. M. T. Puccio,⁷⁶ H. R. Band,⁷⁷ S. Dasu,⁷⁷ K. T. Flood,⁷⁷ Y. Pan,⁷⁷ R. Prepost,⁷⁷ C. O. Vuosalo,⁷⁷ and S. L. Wu⁷⁷

¹*Laboratoire d'Annecy-le-Vieux de Physique des Particules (LAPP), USA Université de Savoie, CNRS/IN2P3, F-74941 Annecy-Le-Vieux, France*

²*Universitat de Barcelona, Facultat de Física, Departament ECM, E-08028 Barcelona, Spain*

^{3a}*INFN Sezione di Bari, I-70126 Bari, Italy*

^{3b}*Dipartimento di Fisica, Università di Bari, I-70126 Bari, Italy*

⁴*University of Bergen, Institute of Physics, N-5007 Bergen, Norway*

⁵*Lawrence Berkeley National Laboratory and University of California, Berkeley, California 94720, USA*

⁶*Ruhr Universität Bochum, Institut für Experimentalphysik I, D-44780 Bochum, Germany*

⁷*University of British Columbia, Vancouver, British Columbia, Canada V6T 1Z1*

⁸*Brunel University, Uxbridge, Middlesex UB8 3PH, United Kingdom*

⁹*Budker Institute of Nuclear Physics, Novosibirsk 630090, Russia*

¹⁰*University of California at Irvine, Irvine, California 92697, USA*

¹¹*University of California at Riverside, Riverside, California 92521, USA*

¹²*University of California at Santa Barbara, Santa Barbara, California 93106, USA*

¹³*University of California at Santa Cruz, Institute for Particle Physics, Santa Cruz, California 95064, USA*

¹⁴*California Institute of Technology, Pasadena, California 91125, USA*

¹⁵*University of Cincinnati, Cincinnati, Ohio 45221, USA*

¹⁶*University of Colorado, Boulder, Colorado 80309, USA*

¹⁷*Colorado State University, Fort Collins, Colorado 80523, USA*

¹⁸*Technische Universität Dortmund, Fakultät Physik, D-44221 Dortmund, Germany*

¹⁹*Technische Universität Dresden, Institut für Kern- und Teilchenphysik, D-01062 Dresden, Germany*

²⁰*Laboratoire Leprince-Ringuet, CNRS/IN2P3, Ecole Polytechnique, F-91128 Palaiseau, France*

²¹*University of Edinburgh, Edinburgh EH9 3JZ, United Kingdom*

^{22a}*INFN Sezione di Ferrara, I-44100 Ferrara, Italy*

^{22b}*Dipartimento di Fisica, Università di Ferrara, I-44100 Ferrara, Italy*

²³*INFN Laboratori Nazionali di Frascati, I-00044 Frascati, Italy*

^{24a}*INFN Sezione di Genova, I-16146 Genova, Italy*

^{24b}*Dipartimento di Fisica, Università di Genova, I-16146 Genova, Italy*

²⁵*Indian Institute of Technology Guwahati, Guwahati, Assam, 781 039, India*

²⁶*Harvard University, Cambridge, Massachusetts 02138, USA*

²⁷*Harvey Mudd College, Claremont, California 91711*

²⁸*Universität Heidelberg, Physikalisches Institut, Philosophenweg 12, D-69120 Heidelberg, Germany*

²⁹*Humboldt-Universität zu Berlin, Institut für Physik, Newtonstr. 15, D-12489 Berlin, Germany*

³⁰*Imperial College London, London, SW7 2AZ, United Kingdom*

³¹*University of Iowa, Iowa City, Iowa 52242, USA*

³²*Iowa State University, Ames, Iowa 50011-3160, USA*

³³*Johns Hopkins University, Baltimore, Maryland 21218, USA*

³⁴*Laboratoire de l'Accélérateur Linéaire, IN2P3/CNRS et Université Paris-Sud 11, Centre Scientifique d'Orsay, B. P. 34, F-91898 Orsay Cedex, France*

³⁵*Lawrence Livermore National Laboratory, Livermore, California 94550, USA*

³⁶*University of Liverpool, Liverpool L69 7ZE, United Kingdom*

³⁷*Queen Mary, University of London, London, E1 4NS, United Kingdom*

³⁸*University of London, Royal Holloway and Bedford New College, Egham, Surrey TW20 0EX, United Kingdom*

³⁹*University of Louisville, Louisville, Kentucky 40292, USA*

⁴⁰*Johannes Gutenberg-Universität Mainz, Institut für Kernphysik, D-55099 Mainz, Germany*

⁴¹*University of Manchester, Manchester M13 9PL, United Kingdom*

⁴²*University of Maryland, College Park, Maryland 20742, USA*

⁴³*University of Massachusetts, Amherst, Massachusetts 01003, USA*

⁴⁴*Massachusetts Institute of Technology, Laboratory for Nuclear Science, Cambridge, Massachusetts 02139, USA*

- ⁴⁵McGill University, Montréal, Québec, Canada H3A 2T8
^{46a}INFN Sezione di Milano, I-20133 Milano, Italy
^{46b}Dipartimento di Fisica, Università di Milano, I-20133 Milano, Italy
⁴⁷University of Mississippi, University, Mississippi 38677, USA
⁴⁸Université de Montréal, Physique des Particules, Montréal, Québec, Canada H3C 3J7
^{49a}INFN Sezione di Napoli, I-80126 Napoli, Italy
^{49b}Dipartimento di Scienze Fisiche, Università di Napoli Federico II, I-80126 Napoli, Italy
⁵⁰NIKHEF, National Institute for Nuclear Physics and High Energy Physics,
 NL-1009 DB Amsterdam, The Netherlands
⁵¹University of Notre Dame, Notre Dame, Indiana 46556, USA
⁵²Ohio State University, Columbus, Ohio 43210, USA
⁵³University of Oregon, Eugene, Oregon 97403, USA
^{54a}INFN Sezione di Padova, I-35131 Padova, Italy
^{54b}Dipartimento di Fisica, Università di Padova, I-35131 Padova, Italy
⁵⁵Laboratoire de Physique Nucléaire et de Hautes Energies, IN2P3/CNRS, Université Pierre et Marie-Curie-Paris6,
 Université Denis Diderot-Paris7, F-75252 Paris, France
^{56a}INFN Sezione di Perugia, I-06100 Perugia, Italy
^{56b}Dipartimento di Fisica, Università di Perugia, I-06100 Perugia, Italy
^{57a}INFN Sezione di Pisa, I-56127 Pisa, Italy
^{57b}Dipartimento di Fisica, Università di Pisa, I-56127 Pisa, Italy
^{57c}Scuola Normale Superiore di Pisa, I-56127 Pisa, Italy
⁵⁸Princeton University, Princeton, New Jersey 08544, USA
^{59a}INFN Sezione di Roma, I-00185 Roma, Italy
^{59b}Dipartimento di Fisica, Università di Roma La Sapienza, I-00185 Roma, Italy
⁶⁰Universität Rostock, D-18051 Rostock, Germany
⁶¹Rutherford Appleton Laboratory, Chilton, Didcot, Oxon, OX11 0QX, United Kingdom
⁶²CEA, Irfu, SPP, Centre de Saclay, F-91191 Gif-sur-Yvette, France
⁶³SLAC National Accelerator Laboratory, Stanford, California 94309 USA
⁶⁴University of South Carolina, Columbia, South Carolina 29208, USA
⁶⁵Southern Methodist University, Dallas, Texas 75275, USA
⁶⁶Stanford University, Stanford, California 94305-4060, USA
⁶⁷State University of New York, Albany, New York 12222, USA
⁶⁸Tel Aviv University, School of Physics and Astronomy, Tel Aviv, 69978, Israel
⁶⁹University of Tennessee, Knoxville, Tennessee 37996, USA
⁷⁰University of Texas at Austin, Austin, Texas 78712, USA
⁷¹University of Texas at Dallas, Richardson, Texas 75083, USA
^{72a}INFN Sezione di Torino, I-10125 Torino, Italy
^{72b}Dipartimento di Fisica Sperimentale, Università di Torino, I-10125 Torino, Italy
^{73a}INFN Sezione di Trieste, I-34127 Trieste, Italy
^{73b}Dipartimento di Fisica, Università di Trieste, I-34127 Trieste, Italy
⁷⁴IFIC, Universitat de Valencia-CSIC, E-46071 Valencia, Spain
⁷⁵University of Victoria, Victoria, British Columbia, Canada V8W 3P6
⁷⁶Department of Physics, University of Warwick, Coventry CV4 7AL, United Kingdom
⁷⁷University of Wisconsin, Madison, Wisconsin 53706, USA
 (Received 5 January 2011; published 6 September 2011)

We study the reactions $e^+e^- \rightarrow e^+e^-\eta^{(\prime)}$ in the single-tag mode and measure the $\gamma\gamma^* \rightarrow \eta^{(\prime)}$ transition form factors in the momentum-transfer range from 4 to 40 GeV². The analysis is based on 469 fb⁻¹ of integrated luminosity collected at PEP-II with the BABAR detector at e^+e^- center-of-mass energies near 10.6 GeV.

DOI: 10.1103/PhysRevD.84.052001

PACS numbers: 14.40.Be, 12.38.Qk, 13.40.Gp

*Now at Temple University, Philadelphia, PA 19122, USA

†Also with Università di Perugia, Dipartimento di Fisica, Perugia, Italy

‡Also with Università di Roma La Sapienza, I-00185 Roma, Italy

§Now at University of South Alabama, Mobile, AL 36688, USA

|| Also with Università di Sassari, Sassari, Italy

I. INTRODUCTION

In this article we report results from studies of the $\gamma^* \gamma^* \rightarrow P$ transition form factors, where P is a pseudoscalar meson. In our previous works [1,2], the two-photon fusion reaction

$$e^+ e^- \rightarrow e^+ e^- P, \quad (1)$$

illustrated by Fig. 1, was used to measure the π^0 and η_c transition form factors. Here, this technique is applied to study the η and η' form factors. The transition form factor describes the effect of the strong interaction on the $\gamma^* \gamma^* \rightarrow P$ transition. It is a function, $F(q_1^2, q_2^2)$, of the photon virtualities q_i^2 . We measure the differential cross sections for the processes $e^+ e^- \rightarrow e^+ e^- \eta^{(\prime)}$ in the single tag mode where one of the outgoing electrons¹ (tagged) is detected while the other (untagged) is scattered at a small angle. The tagged electron emits a highly off-shell photon with the momentum transfer $q_1^2 \equiv -Q^2 = (p - p')^2$, where p and p' are the four-momenta of the initial and final electrons. The momentum transfer to the untagged electron (q_2^2) is near zero. The form factor extracted from the single tag experiment is a function of one of the q^2 's: $F(Q^2) \equiv F(-Q^2, 0)$. To relate the differential cross section $d\sigma(e^+ e^- \rightarrow e^+ e^- P)/dQ^2$ to the transition form factor, we use formulae equivalent to those for the $e^+ e^- \rightarrow e^+ e^- \pi^0$ cross section in Eqs. (2.1) and (4.5) of Ref. [3].

At large momentum transfer, perturbative QCD predicts that the transition form factor can be represented as a convolution of a calculable hard-scattering amplitude for $\gamma \gamma^* \rightarrow q \bar{q}$ with a nonperturbative meson distribution amplitude (DA) $\phi_P(x, Q^2)$ [4]. The latter can be interpreted as the amplitude for the transition of the meson with momentum p_M into two quarks with momenta $p_M x$ and $p_M(1-x)$. The experimentally derived photon-meson transition form factors can be used to test different models for the DA.

The η and η' transition form factors have been measured in two-photon reactions in several previous experiments [5–9]. The most precise data for the $\eta^{(\prime)}$ at large Q^2 were obtained by the CLEO experiment [9]. They cover the Q^2 region from 1.5 to about 20 GeV². In this article, we study the η and η' form factors in the Q^2 range from 4 to 40 GeV².

II. THE BABAR DETECTOR AND DATA SAMPLES

We analyze a data sample corresponding to an integrated luminosity of about 469 fb⁻¹ recorded with the BABAR detector [10] at the PEP-II asymmetric-energy storage rings at the SLAC National Accelerator Laboratory. At PEP-II, 9-GeV electrons collide with 3.1-GeV positrons to yield a center-of-mass (c.m.) energy near 10.58 GeV

¹Unless otherwise specified, we use the term “electron” for either an electron or a positron.

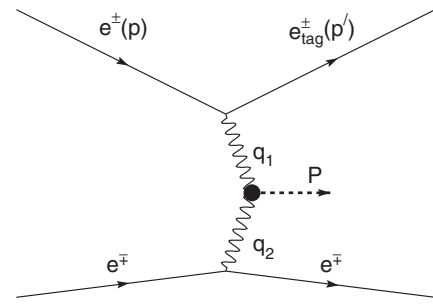


FIG. 1. The diagram for the $e^+ e^- \rightarrow e^+ e^- P$ two-photon production process, where P is a pseudoscalar meson.

(i.e., the $Y(4S)$ resonance peak). About 90% of the data used in the present analysis were recorded on-resonance and about 10% were recorded about 40 MeV below the resonance.

Charged-particle tracking is provided by a five-layer silicon vertex tracker and a 40-layer drift chamber, operating in a 1.5-T axial magnetic field. The transverse momentum resolution is 0.47% at 1 GeV/ c . Energies of photons and electrons are measured with a CsI(Tl) electromagnetic calorimeter with a resolution of 3% at 1 GeV. Charged-particle identification is provided by specific ionization (dE/dx) measurements in the vertex tracker and drift chamber and by an internally reflecting ring-imaging Cherenkov detector. Electron identification also makes use of the shower shape in the calorimeter and the ratio of shower energy to track momentum. Muons are identified in the instrumented flux return of the solenoid, which consists of iron plates interleaved with either resistive plate chambers or streamer tubes.

Signal $e^+ e^- \rightarrow e^+ e^- \eta^{(\prime)}$ and two-photon background processes are simulated with the Monte Carlo (MC) event generator GGResRc [11]. It uses the formula for the differential cross section from Ref. [3] for pseudoscalar meson production and the Budnev-Ginzburg-Meledin-Serbo formalism [12] for the two-meson final states. Because the Q^2 distribution is peaked near zero, the MC events are generated with a restriction on the momentum transfer to one of the electrons: $Q^2 > 3$ GeV². This restriction corresponds to the limit of detector acceptance for the tagged electron. The second electron is required to have momentum transfer $-q_2^2 < 0.6$ GeV². The experimental criteria providing these restrictions for data events will be described in Sec. III. The form factor is fixed to the constant value $F(0, 0)$ in the simulation.

The GGResRc event generator includes next-to-leading-order radiative corrections to the Born cross section calculated according to Ref. [13]. In particular, it generates extra soft photons emitted by the initial- and final-state electrons. The formulae from Ref. [13] are modified to take into account the hadron contribution to the vacuum polarization diagrams. The maximum energy of the photon emitted

from the initial state is restricted by the requirement² $E_\gamma^* < 0.05\sqrt{s}$, where \sqrt{s} is the e^+e^- c.m. energy. The generated events are subjected to a detailed detector simulation based on GEANT4 [14] and are reconstructed with the software chain used for the experimental data. Temporal variations in the detector performance and beam background conditions are taken into account.

III. EVENT SELECTION

The decay modes with two charged particles and two photons in the final state, $\eta' \rightarrow \pi^+\pi^-\eta$, $\eta \rightarrow \gamma\gamma$ and $\eta \rightarrow \pi^+\pi^-\pi^0$, $\pi^0 \rightarrow \gamma\gamma$, are used to reconstruct η' and η mesons, respectively. For the $e^+e^- \rightarrow e^+e^-\eta$ process, $\eta \rightarrow \pi^+\pi^-\pi^0$ is the only decay mode available for analysis at BABAR. The trigger efficiency for events with η decays to 2γ and to $3\pi^0$ is very low.

Events with at least three charged tracks and two photons are selected. Since a significant fraction of signal events contains beam-generated spurious track and photon candidates, one extra track and any number of extra photons are allowed in an event. The tracks corresponding to the charged pions and electron must have a point of closest approach to the nominal interaction point (IP) that is within 2.5 cm along the beam axis and less than 1.5 cm in the transverse plane. The track transverse momentum must be greater than 50 MeV/c. The identified pion candidates must have polar angles in the range $25.8^\circ < \theta < 137.5^\circ$, while the track identified as an electron must be in the angular range $22.2^\circ < \theta < 137.5^\circ$ ($36.7\text{--}154.1^\circ$ in the e^+e^- c.m. frame). The angular requirements are needed for good electron and pion identification. Electrons and pions are selected using a likelihood based identification algorithm, which combines the measurements of the tracking system, the Cherenkov detector, and the electromagnetic calorimeter. The electron identification efficiency is about 98–99%, with a pion-misidentification probability below 10%. The pions are identified with about 98% efficiency and a electron-misidentification rate of about 7%. To recover electron energy loss due to bremsstrahlung, both internal and in the detector material before the drift chamber, the energy of any calorimeter shower close to the electron direction (within 35 and 50 mrad for the polar and azimuthal angle, respectively) is combined with the measured energy of the electron track. The resulting c.m. energy of the electron candidate must be greater than 1 GeV.

The photon candidates are required to have laboratory energies greater than 50 MeV. For the $e^+e^- \rightarrow e^+e^-\eta'$ selection, two photon candidates are combined to form an η candidate. Their invariant mass is required to be in the range 0.480–0.600 GeV/c². To suppress combinatorial

²Throughout this article, an asterisk superscript denotes quantities in the e^+e^- c.m. frame. In this frame, the positive z-axis is defined to coincide with the e^- beam direction.

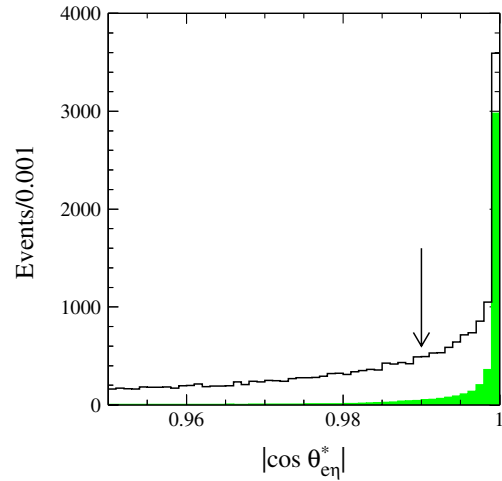


FIG. 2 (color online). The $|\cos\theta_{e\eta}^*|$ distribution for data events (solid histogram). The shaded histogram shows the same distributions for the $e^+e^- \rightarrow e^+e^-\eta$ simulation. Events with $|\cos\theta_{e\eta}^*| > 0.99$ (indicated by the arrow) are retained.

background from spurious photons, the photon helicity angle is required to satisfy the condition $|\cos\theta_h| < 0.9$.³ The helicity angle θ_h is defined in the η rest frame as the angle between the decay photon momentum and direction of the boost from the laboratory frame. Each candidate is then fit with an η -mass constraint to improve the precision of its momentum measurement. An η' candidate is formed from a pair of oppositely-charged pion candidates and an η candidate. The η' invariant mass must be in the range 0.920–0.995 GeV/c². The η' candidate is also then fit with a mass constraint.

Similar selection criteria are used for $e^+e^- \rightarrow e^+e^-\eta$ candidates. An η candidate is formed from a pair of oppositely charged pion candidates and a π^0 candidate, which is a combination of two photons with invariant mass between 0.115 and 0.150 GeV/c² and the cosine of the photon helicity angle $|\cos\theta_h| < 0.9$. The mass of the η candidate must be in the selection region 0.48–0.62 GeV/c².

Figure 2 shows the $|\cos\theta_{e\eta}^*|$ distribution for data and simulated $e^+e^- \rightarrow e^+e^-\eta$ events passing the selection criteria described above, where $\theta_{e\eta}^*$ is the polar angle of the momentum vector of the $e\eta$ system in the e^+e^- c.m. frame. We require that $|\cos\theta_{e\eta}^*|$ be greater than 0.99. This condition effectively limits the value of the momentum transfer to the untagged electron (q_2^2) and guarantees compliance with the condition $-q_2^2 < 0.6$ GeV² used in the MC simulation. The same condition $|\cos\theta_{e\eta}^*| > 0.99$ is used to select the $e^+e^- \rightarrow e^+e^-\eta'$ event candidates.

³Spurious photons tend to have low energy, and therefore align opposite to the η/π^0 candidate's boost direction, whereas true η/π^0 meson decays into two photons have a flat $\cos\theta_h$ distribution.

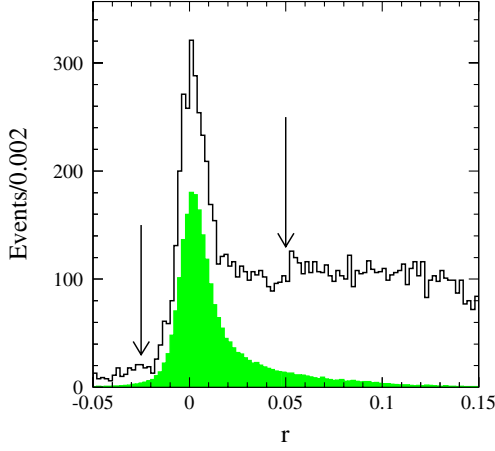


FIG. 3 (color online). The r distributions for $e^+e^- \rightarrow e^+e^-\eta$ data (solid-line histogram) and signal simulation (shaded histogram). The arrows indicate the region used to select event candidates ($-0.025 < r < 0.05$).

The emission of extra photons by the electrons involved leads to a difference between the measured and actual values of Q^2 . In the case of initial-state radiation (ISR) $Q_{\text{meas}}^2 = Q_{\text{true}}^2(1 + r_\gamma)$, where $r_\gamma = 2E_\gamma^*/\sqrt{s}$. To restrict the energy of the ISR photon we use the parameter

$$r = \frac{\sqrt{s} - E_{e\eta^{(l)}}^* - |p_{e\eta^{(l)}}^*|}{\sqrt{s}}, \quad (2)$$

where $E_{e\eta^{(l)}}^*$ and $p_{e\eta^{(l)}}^*$ are the c.m. energy and momentum of the detected $e\eta^{(l)}$ system. For ISR, this parameter coincides with r_γ defined above. The r distributions for data and simulated $e^+e^- \rightarrow e^+e^-\eta$ events passing the selection criteria described above are shown in Fig. 3. For both processes under study, we select events with $-0.025 < r < 0.05$. It should be noted that this condition on r ensures

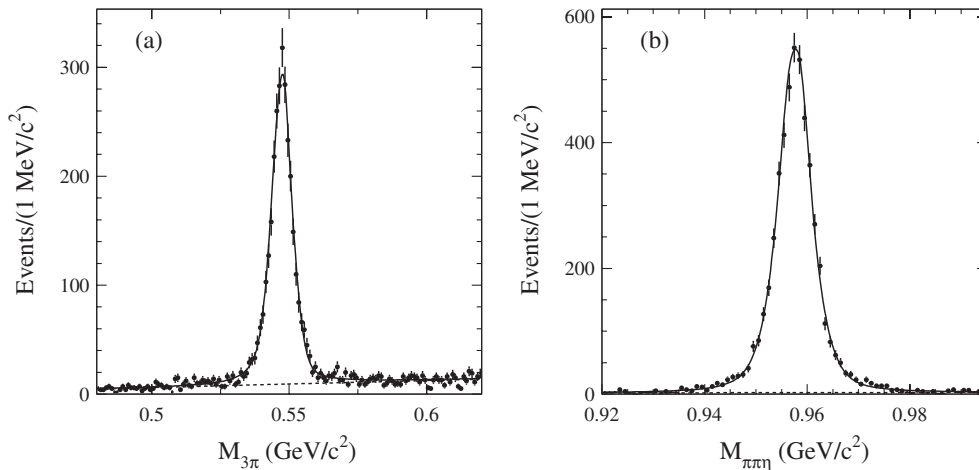


FIG. 4. The (a) $\pi^+\pi^-\pi^0$ and (b) $\pi^+\pi^-\eta$ mass spectra for data events with $4 < Q^2 < 40 \text{ GeV}^2$. The solid curves are the results of the fits described in Sec. IV. The dashed curves represent non-peaking background.

compliance with the restriction $r_\gamma < 0.1$ used in the simulation.

For two-photon events with a tagged positron (electron), the momentum of the detected $e\eta^{(l)}$ system in the e^+e^- c.m. frame has a negative (positive) z -component, while events resulting from e^+e^- annihilation are produced symmetrically. To suppress the e^+e^- annihilation background, event candidates with the wrong sign of the momentum z -component are removed.

The distributions of the invariant masses of η and η' candidates for data events satisfying the selection criteria described above are shown in Fig. 4. For events with more than one $e^\pm\eta^{(l)}$ candidate (about 5% of the selected events), the candidate with smallest absolute value of the parameter r is selected. Only events with $4 < Q^2 < 40 \text{ GeV}^2$ are included in the spectra of Fig. 4. For $Q^2 < 4 \text{ GeV}^2$, the detection efficiency for single-tag two-photon η and η' events is small (see Sec. VI). In the region $Q^2 > 40 \text{ GeV}^2$, we do not see evidence of η or η' signal over background. About 4350 and 5200 events survive the selection described above for η and η' , respectively.

IV. FITTING THE $\pi^+\pi^-\pi^0$ AND $\pi^+\pi^-\eta$ MASS SPECTRA

To determine the number of events containing an $\eta^{(l)}$, we perform a binned likelihood fit to the spectra shown in Fig. 4 with a sum of signal and background distributions. The signal distributions are obtained by fitting mass spectra for simulated signal events. The obtained functions then are modified to take into account a possible difference between data and simulation in detector response. The signal line shape in simulation is described by the following function:

$$F(x) = A[G(x)\sin^2\zeta + B(x)\cos^2\zeta], \quad (3)$$

where

$$G(x) = \exp\left(-\frac{(x-a)^2}{2\sigma^2}\right), \quad (4)$$

$$B(x) = \begin{cases} \frac{(\Gamma_1/2)^{\beta_1}}{(a-x)^{\beta_1} + (\Gamma_1/2)^{\beta_1}} & \text{if } x < a; \\ \frac{(\Gamma_2/2)^{\beta_2}}{(x-a)^{\beta_2} + (\Gamma_2/2)^{\beta_2}} & \text{if } x \geq a, \end{cases} \quad (5)$$

ζ , a , σ , Γ_1 , β_1 , Γ_2 , and β_2 are resolution function parameters, and A is a normalization factor. The $B(x)$ term is added to the Gaussian function to describe the asymmetric power-law tails of the detector resolution function. The mass spectra for simulated signal events weighted to yield the Q^2 dependencies observed in data and fitted curves are shown in Fig. 5.

When used in data, the parameters σ , Γ_1 , Γ_2 and a are modified to account for possible differences between data and simulation in resolution ($\Delta\sigma$) and mass scale calibration (Δa):

$$\sigma^2 = \begin{cases} \sigma_{\text{MC}}^2 - \Delta\sigma^2 & \text{if } \Delta\sigma < 0; \\ \sigma_{\text{MC}}^2 + \Delta\sigma^2 & \text{if } \Delta\sigma \geq 0, \end{cases} \quad (6)$$

$$\Gamma_i^2 = \begin{cases} \Gamma_{i,\text{MC}}^2 - (2.35\Delta\sigma)^2 & \text{if } \Delta\sigma < 0; \\ \Gamma_{i,\text{MC}}^2 + (2.35\Delta\sigma)^2 & \text{if } \Delta\sigma \geq 0, \end{cases} \quad (7)$$

$$a = a_{\text{MC}} + \Delta a, \quad (8)$$

where the subscript MC indicates the parameter value determined from the fit to the simulated mass spectrum. The resolution and mass differences, $\Delta\sigma$ and Δa , are determined by a fit to data.

The background distribution is described by a linear function. Five parameters are determined in the fit to the measured mass spectrum: the number of $\eta^{(\prime)}$ events, Δa ,

$\Delta\sigma$, and two background shape parameters. The fitted curves are shown in Fig. 4. The numbers of η and η' events are found to be 3060 ± 70 and 5010 ± 90 , respectively. The mass shifts are $\Delta a = 0.25 \pm 0.09 \text{ MeV}/c^2$ for the η and $\Delta a = -(0.48 \pm 0.06) \text{ MeV}/c^2$ for the η' . To check possible dependence of the mass shift on Q^2 , separate fits are performed for two Q^2 regions: $4 < Q^2 < 10 \text{ GeV}^2$ and $10 < Q^2 < 40 \text{ GeV}^2$. The Δa values obtained for these regions agree with each other both for η and η' . In contrast, the values of $\Delta\sigma$ are found to be strongly dependent on Q^2 , changing from $0.9 \pm 0.3 \text{ MeV}/c^2$ for $4 < Q^2 < 10 \text{ GeV}^2$ to $-(1.0 \pm 0.6) \text{ MeV}/c^2$ for $10 < Q^2 < 40 \text{ GeV}^2$. It should be noted that the mass resolution for η and η' is about $4 \text{ MeV}/c^2$. The data-MC difference, $\Delta\sigma \sim 1 \text{ MeV}/c^2$, corresponds to a small ($\sim 3\%$) change in the mass resolution when added in quadrature.

A fitting procedure similar to that described above is applied in each of the 11 Q^2 intervals indicated in Table I. The parameters of the mass resolution function are taken from the fit to the mass spectrum for simulated events in the corresponding Q^2 interval. The η and η' masses are fixed to the values obtained from the fit to the spectra of Fig. 4. The $\Delta\sigma$ parameter is set to zero. Fits with $\Delta\sigma = 0.9 \text{ MeV}/c^2$ and $\Delta\sigma = -1.0 \text{ MeV}/c^2$ are also performed. The differences between the results of the fits with zero and nonzero $\Delta\sigma$ provide an estimate of the systematic uncertainty associated with the data-MC simulation difference in the detector mass resolution.

For the analysis of the $e^+e^- \rightarrow e^+e^-\eta$ process, the numbers of events containing an η are determined in two regions of the parameter r : $-0.025 < r < 0.025$ (N_1) and $0.025 < r < 0.050$ (N_2). The N_1 and N_2 values are used to determine the numbers of signal events (N_s) and background events peaking at the η mass (N_b) as described in Sec. V. These values are listed in Table I. The $\pi^+\pi^-\pi^0$ mass spectra and fitted curves for three representative Q^2 intervals are shown in Fig. 6. The spectra shown are

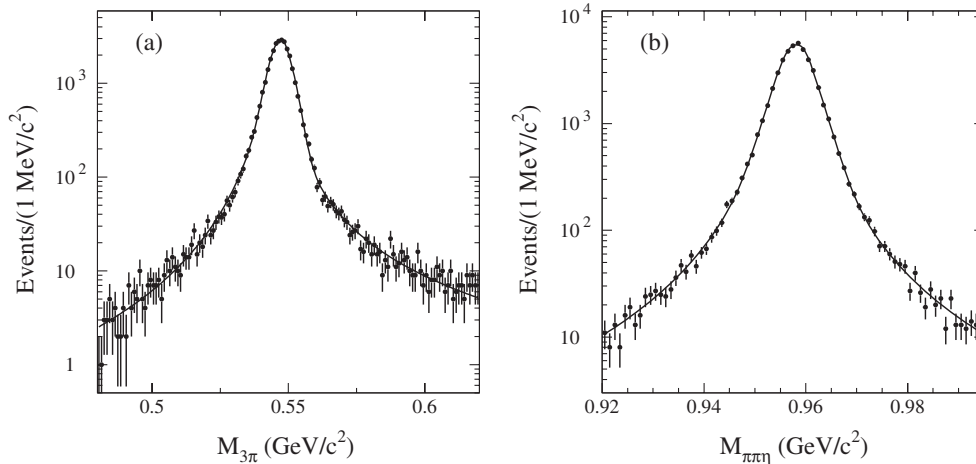


FIG. 5. The $\pi^+\pi^-\pi^0$ and $\pi^+\pi^-\eta$ mass spectra for simulated (a) $e^+e^- \rightarrow e^+e^-\eta$ and (b) $e^+e^- \rightarrow e^+e^-\eta'$ events, respectively. The curves represent the resolution functions described in the text.

TABLE I. The Q^2 interval, number of detected $e^+e^- \rightarrow e^+e^-\eta$ signal events (N_s), number of peaking-background events (N_b), efficiency correction (δ_{total}), number of signal events corrected for data-MC difference and resolution effects ($N_{\text{corr}}^{\text{unfolded}}$), and detection efficiency obtained from simulation (ε). The first and second errors on N_s and $N_{\text{corr}}^{\text{unfolded}}$ are statistical and systematic, respectively. The errors on N_b are statistical and systematic combined in quadrature.

Q^2 interval (GeV ²)	N_s	N_b	δ_{total} (%)	$N_{\text{corr}}^{\text{unfolded}}$	ε (%)
4–5	638 ± 31 ± 16	53 ± 27	−1.4	634 ± 34 ± 18	6.3
5–6	625 ± 34 ± 19	89 ± 34	−1.6	641 ± 38 ± 22	13.0
6–8	622 ± 36 ± 23	97 ± 37	−1.7	634 ± 39 ± 25	14.7
8–10	349 ± 26 ± 12	43 ± 23	−2.0	359 ± 29 ± 14	18.7
10–12	212 ± 20 ± 7	15 ± 16	−2.3	224 ± 22 ± 8	22.6
12–14	104 ± 14 ± 4	13 ± 11	−2.1	105 ± 17 ± 5	22.9
14–17	109 ± 13 ± 3	0.0 ± 9.2	−2.0	116 ± 15 ± 4	22.2
17–20	40.5 ± 8.3 ± 1.2	0.7 ± 5.6	−2.3	41.2 ± 9.5 ± 1.4	21.3
20–25	32.5 ± 7.4 ± 0.8	0.0 ± 4.2	−2.4	34.4 ± 8.3 ± 0.9	19.6
25–30	13.7 ± 5.3 ± 0.5	3.1 ± 3.5	−2.7	14.2 ± 6.0 ± 0.6	18.0
30–40	13.0 ± 4.8 ± 0.3	0.5 ± 3.7	−2.7	14.1 ± 5.3 ± 0.3	15.7

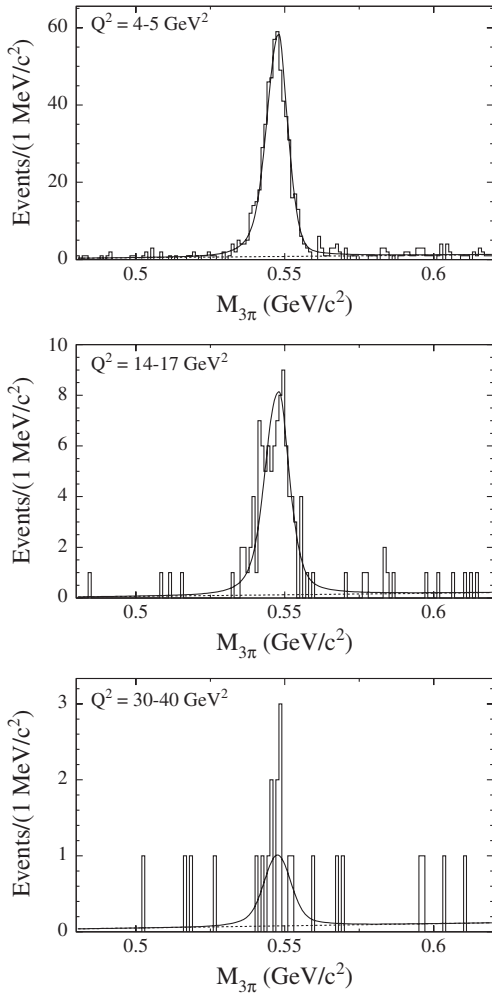


FIG. 6. The $\pi^+\pi^-\pi^0$ mass spectra for data events with $-0.025 < r < 0.025$ for three representative Q^2 intervals. The solid curves are the fit results. The dashed curves represent non-peaking background.

obtained for the $-0.025 < r < 0.025$ regions; the $0.025 < r < 0.050$ regions contain only 10–13% of the signal events and are used mainly to estimate backgrounds.

For the $e^+e^- \rightarrow e^+e^-\eta'$ process, background is assumed to be small. There is no need to separate events into two r regions. The $\pi^+\pi^-\eta$ mass spectra and fitted curves for three representative Q^2 intervals are shown in Fig. 7. The numbers of signal η' events obtained from the fits are listed in Table II.

V. PEAKING BACKGROUND ESTIMATION AND SUBTRACTION

Background events containing true η or η' mesons might arise from e^+e^- annihilation, and two-photon processes with higher multiplicity final states than our signal events. The e^+e^- annihilation background is studied in Sec. VA. In Sec. VB, we use events with an extra π^0 to estimate the level of the two-photon background and study its characteristics. In Sec. VC we develop a method of background subtraction based on the difference in the r distributions for signal and background events. This method gives an improvement in accuracy compared to the previous one described in Sec. VB and has a lower sensitivity to the model used for background simulation.

A. e^+e^- annihilation background

The background from e^+e^- annihilation can be estimated using events with the wrong sign of the $e^\pm \eta^{(\prime)}$ momentum z -component. The numbers of background events from e^+e^- annihilation in the wrong- and right-sign data samples are expected to be approximately the same, but their Q^2 distributions are quite different. The Q^2 distribution expected for right-sign background events coincides with the Q_{ws}^2 distribution for wrong-sign events, where Q_{ws}^2 is the squared difference between the

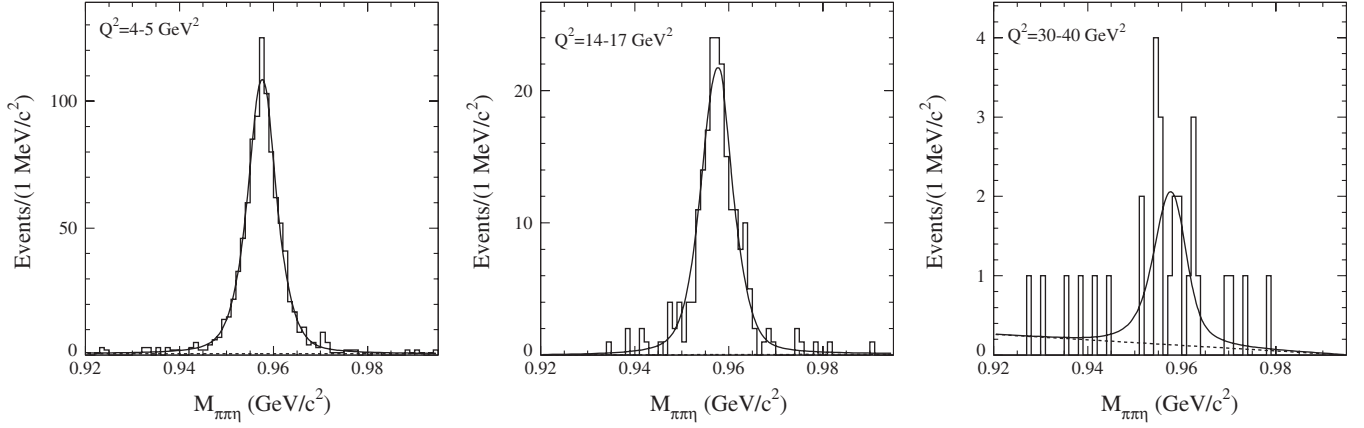


FIG. 7. The $\pi^+ \pi^- \eta$ mass spectra for data events for three representative Q^2 intervals. The solid curves are the fit results. The dashed lines represent non-peaking background.

four-momenta of the detected positron (electron) and the initial electron (positron).

In the Q_{ws}^2 region from 4 to 40 GeV^2 , we observe three wrong-sign events in the η' data sample, all peaking at the η' mass, and nine events in the η data sample, five of which are in the 0.530–0.565 GeV/c^2 mass window. The contribution from non- η events to this mass window is estimated to be 0.3 events. A possible source of these events is the $e^+ e^- \rightarrow X \gamma$ process, where X is a hadronic system containing an η or η' meson, for example, $\pi^+ \pi^- \eta'$, with the photon emitted along the beam axis.

The Q_{ws}^2 distribution for the wrong-sign events is used to estimate the Q^2 distribution for $e^+ e^-$ annihilation background in the right-sign data sample. The fraction of $e^+ e^-$ annihilation events in the $\eta^{(\prime)}$ data sample is about 10^{-3} . However, such events are the main contribution to the peaking background in high Q^2 bins and cannot be neglected. For the $e^+ e^- \rightarrow e^+ e^- \eta^{(\prime)}$ process, for which we do not observe a significant two-photon background (see Sec. VB), the three background events from $e^+ e^-$

annihilation are subtracted from the two highest Q^2 intervals (see Table II).

For the $e^+ e^- \rightarrow e^+ e^- \eta$ process, the $e^+ e^-$ annihilation events are effectively subtracted with the procedure developed for subtraction of two-photon background (see Sec. VC). The procedure exploits the difference between the r distributions for signal and background events. The r distribution for the $e^+ e^-$ annihilation events (3 of 5 events have $r > 0.025$) is close to that for two-photon background.

In future high statistics, measurements of the meson-photon form factors at Super B factories $e^+ e^-$ annihilation will be the dominant background in the high Q^2 region ($Q^2 \gtrsim 50 \text{ GeV}^2$).

B. Two-photon background

Other possible sources of peaking background are the two-photon processes $e^+ e^- \rightarrow e^+ e^- \eta^{(\prime)} \pi^0$. For the η selection the additional background comes from the two-photon production of η' mesons followed by the decay

TABLE II. The Q^2 interval, number of detected η' signal events (N_s), number of peaking-background events (N_b), efficiency correction (δ_{total}), number of signal events corrected for data-MC difference and resolution effects ($N_{\text{corr}}^{\text{unfolded}}$), and detection efficiency obtained from simulation (ε). The first and second errors on N_s and $N_{\text{corr}}^{\text{unfolded}}$ are statistical and systematic, respectively.

Q^2 interval (GeV^2)	N_s	N_b	$\delta_{\text{total}}(\%)$	$N_{\text{corr}}^{\text{unfolded}}$	$\varepsilon(\%)$
4–5	$950 \pm 32 \pm 5$	0.0 ± 0.0	–0.4	$936 \pm 34 \pm 6$	5.7
5–6	$1013 \pm 33 \pm 6$	0.0 ± 0.0	–0.6	$1015 \pm 36 \pm 7$	12.5
6–8	$1185 \pm 36 \pm 5$	0.0 ± 0.0	–0.7	$1207 \pm 38 \pm 6$	14.3
8–10	$710 \pm 28 \pm 3$	0.0 ± 0.0	–1.0	$716 \pm 30 \pm 4$	19.9
10–12	$454 \pm 22 \pm 4$	0.0 ± 0.0	–1.2	$467 \pm 25 \pm 4$	26.4
12–14	$243 \pm 16 \pm 1$	0.0 ± 0.0	–1.0	$250 \pm 19 \pm 1$	28.1
14–17	$207 \pm 15 \pm 2$	0.0 ± 0.0	–0.8	$214 \pm 17 \pm 2$	28.1
17–20	$108 \pm 10 \pm 1$	0.0 ± 0.0	–0.8	$112 \pm 12 \pm 1$	26.8
20–25	$80.0 \pm 9.0 \pm 0.1$	0.0 ± 0.0	–1.0	$82.5 \pm 9.9 \pm 0.2$	26.3
25–30	$30.2 \pm 5.9 \pm 0.2$	1.0 ± 1.0	–1.3	$31.7 \pm 6.7 \pm 0.2$	25.6
30–40	$17.2 \pm 5.4 \pm 0.1$	2.0 ± 1.4	–1.4	$18.1 \pm 5.8 \pm 0.1$	22.5

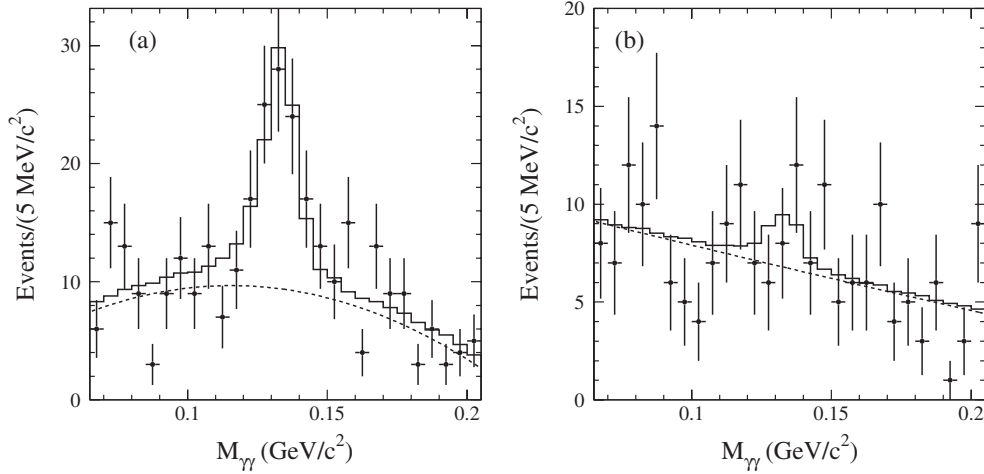


FIG. 8. The two-photon invariant mass spectra for (a) η and (b) η' events with two extra photons. The solid histograms represent the fit results. The dashed curves are the fitted distributions for events without an extra π^0 .

chain $\eta' \rightarrow \pi^0 \pi^0 \eta$, $\eta \rightarrow \pi^+ \pi^- \pi^0$. The Q^2 distribution of events from the latter background source is calculated from the Q^2 distribution of the selected η' events. The ratio of the detection efficiencies for the two η' decay modes is obtained from MC simulation. The total number of $\eta' \rightarrow \pi^0 \pi^0 \eta$ events in the η data sample is estimated to be 17 ± 2 . The events are concentrated almost entirely in the three lowest Q^2 bins.

To estimate background contributions from the $e^+e^- \rightarrow e^+e^-\eta^{(\prime)}\pi^0$ processes, we select events with two extra photons that each have an energy greater than 70 MeV. The distributions of the invariant mass of these extra photons for η and η' events are shown in Fig. 8. The invariant masses of the η and η' candidates are required to be in the mass windows $0.530\text{--}0.565\text{ GeV}/c^2$ and $0.945\text{--}0.970\text{ GeV}/c^2$, respectively. The spectra are fit by a sum of the π^0 line shape obtained from simulated $e^+e^- \rightarrow e^+e^-\eta^{(\prime)}\pi^0$ events and a quadratic polynomial. The fitted numbers of events with an extra π^0 are 90 ± 20 and 13 ± 14 for the η and η' selections, respectively. It is expected that eight events with an extra π^0 in the η sample arise from two-photon η' production.

The distribution of the $\eta\pi^0$ invariant mass for events with an extra π^0 is shown in Fig. 9. The two-photon invariant mass of the π^0 candidate is required to be in the $0.115\text{--}0.150\text{ GeV}/c^2$ range. The sidebands, $0.065\text{--}0.100$ and $0.170\text{--}0.205\text{ GeV}/c^2$, are used to subtract contamination from non- $\eta\pi^0$ events. It is known from two-photon measurements in the no-tag mode [15] that the $\eta\pi^0$ final state is produced mainly via $a_0(980)$ and $a_2(1320)$ intermediate resonances. Evidence for these two intermediate resonances is seen in the mass spectrum of Fig. 9. Our spectrum differs significantly from the spectrum for the no-tag mode [15], which is dominated by $a_2(1320)$ production. In the no-tag mode, the $a_2(1320)$ meson is produced predominantly in a helicity-2 state, and thus with an angular distribution proportional to

$\sin^4\theta_\pi$, where θ_π is the angle between the π^0 direction and the $\gamma\gamma$ collision axis in the $\gamma\gamma$ c.m. frame. Our selection criteria favor events with values of θ_π near zero and hence suppress helicity-2 states.

From MC simulation, we estimate that the ratio of the number of $e^+e^- \rightarrow e^+e^-\eta^{(\prime)}\pi^0$ events with a detected π^0 to the number selected with standard criteria is about 2.5. For the $e^+e^- \rightarrow e^+e^-\eta'$ process the estimated two-photon background does not exceed 1.6% of the total number of selected η' events at 90% confidence level. This background level is treated as a measure of the systematic uncertainty due to possible two-photon background for the $e^+e^- \rightarrow e^+e^-\eta'$ process.

For the $e^+e^- \rightarrow e^+e^-\eta$ process, the two-photon background is about 10% of the total number of selected η events. It should be noted that in the CLEO publication [9]

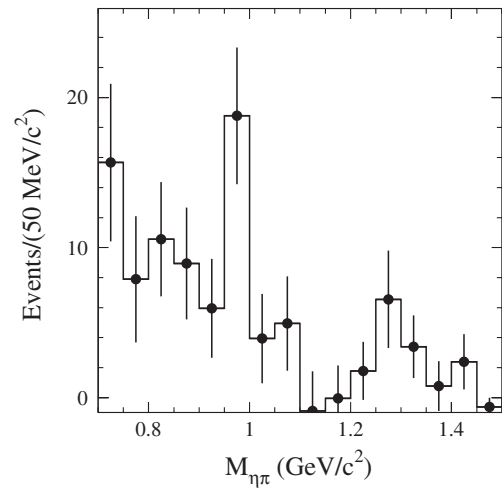


FIG. 9. The distribution of the $\eta\pi^0$ invariant mass for η events with an extra π^0 . The background from non- $\eta\pi^0$ events is subtracted.

on measurements of the meson-photon transition form factors, the background from the two-photon production of the $\eta\pi^0$ final state was not considered.

A similar technique is used to estimate background from the process $e^+e^- \rightarrow e^+e^-\phi$, $\phi \rightarrow \eta\gamma$. We do not see any ϕ meson signal in the $\eta\gamma$ mass spectrum and estimate that this background does not exceed 10% of the $\eta\pi^0$ background. The $\eta\gamma$ events have the r distribution similar to that for $\eta\pi^0$ events, and are effectively subtracted by the procedure described in the next section. The background contributions from the processes $e^+e^- \rightarrow e^+e^-\phi$, $\phi \rightarrow \eta'\gamma$ is negligible due to the small $\phi \rightarrow \eta'\gamma$ branching fraction. The background from $e^+e^- \rightarrow e^+e^-J/\psi$, $J/\psi \rightarrow \eta^{(\prime)}\gamma$ is estimated using the Q^2 distribution of $e^+e^- \rightarrow e^+e^-J/\psi$ events measured in Ref. [2] and efficiencies from MC simulations, and is found to be negligible.

C. Background subtraction from the η data sample

To subtract background from the η data sample, the difference between the r distributions for signal and background events is used. The parameter r is proportional to the difference between the energy and the momentum of particles recoiling against the $e\eta^{(\prime)}$ system and, therefore, is close to zero for signal and has nonzero positive value for background events. To obtain the r distribution, data events are divided into 15 r intervals. For each interval, the fit to the $\pi^+\pi^-\pi^0$ ($\pi^+\pi^-\eta$) spectra is performed and the number of events containing an $\eta^{(\prime)}$ is determined. The r distributions for events in the η and η' data samples are shown in Fig. 10.

For η' events, for which the background is small, the data distribution is compared with the simulated signal distribution normalized to the number of data events. The distributions are in reasonable agreement. The ratio R_s of

the number of events with $r > 0.025$ to the number with $r < 0.025$ is found to be 0.103 ± 0.006 in data and 0.116 ± 0.002 in simulation; the 13% difference is taken as a systematic uncertainty on the R_s value for η' events determined from simulation. Since the simulated r distributions for η' and η events are very close, the same systematic error can be applied to R_s value for η events.

For η events, the data r distribution is fit with the sum of the simulated distributions for signal and background $e^+e^- \rightarrow e^+e^-\eta\pi^0$ and $e^+e^- \rightarrow e^+e^-\eta' \rightarrow e^+e^-\pi^0\pi^0\eta$ events. The fitted number of background events is 280 ± 40 , in reasonable agreement with the estimate given in the previous subsection based on the number of events with a detected extra π^0 .

To subtract the background in each Q^2 interval the following procedure is used. In Sec. IV, we described how the number of events containing an η is determined for two regions of the parameter r : $-0.025 < r < 0.025$ (N_1) and $0.025 < r < 0.050$ (N_2). The numbers of signal and background events are then calculated as follows:

$$N_s = \frac{(1 + R_s)(N_1 R_b - N_2)}{R_b - R_s}, \quad (9)$$

$$N_b = \frac{(1 + R_b)(N_2 - N_1 R_s)}{R_b - R_s}, \quad (10)$$

where R_s (R_b) is the N_2/N_1 ratio obtained from signal (background) MC simulation. The expressions in Eqs. (9) and (10) are equivalent to a two- r -bin fit of data to signal and background MC predictions; fits using a higher number of bins are not useful due to lack of statistics.

The parameter R_s is found to vary from 0.15 to 0.10 with increasing Q^2 . The systematic uncertainty on R_s (13%) was estimated above. To calculate R_b for the

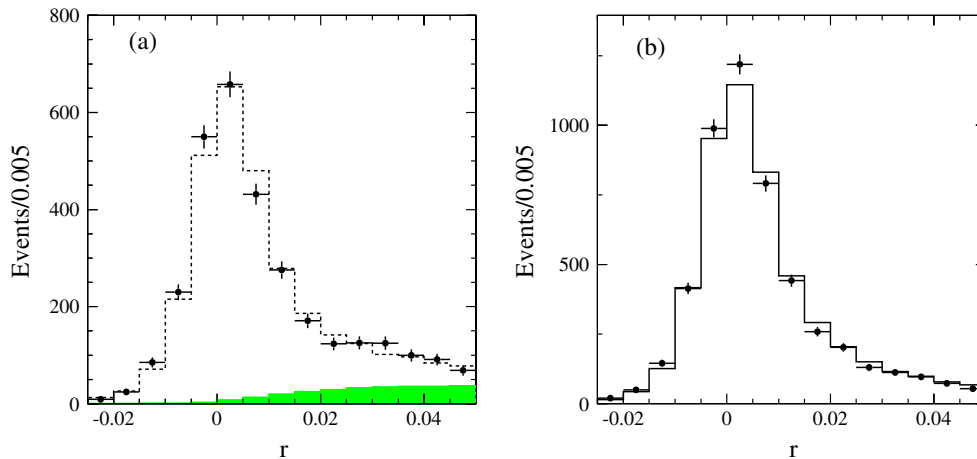


FIG. 10 (color online). (a) The r distribution for data events containing an η (points with error bars). The dashed histogram shows the fit results. The shaded histogram is the fitted background contribution from the processes $e^+e^- \rightarrow e^+e^-\eta\pi^0$ and $e^+e^- \rightarrow e^+e^-\eta' \rightarrow e^+e^-\pi^0\pi^0\eta$. (b) The r distribution for data events containing an η' (points with error bars). The solid histogram is the simulated distribution for events from the signal $e^+e^- \rightarrow e^+e^-\eta'$ process normalized to the number of data events.

$e^+e^- \rightarrow e^+e^-\eta\pi^0$ process, the simulated background events are reweighted to reproduce the $\eta\pi^0$ mass spectrum observed in data (Fig. 9). The R_b value varies from 2.0 to 1.5. The systematic uncertainty on R_b is estimated based on its $\eta\pi^0$ mass dependence. The maximum deviation from the value averaged over the $\eta\pi^0$ spectrum of about 25% is found when we exclude events with mass near the $\eta\pi^0$ threshold. This deviation is taken as an estimate of the systematic uncertainty on R_b . The r distribution for background events from two-photon η' production (R_b is about 10) differs significantly from the distribution for $\eta\pi^0$ events. Therefore, we first subtract the calculated η' contribution from N_1 and N_2 in each Q^2 interval, and then calculate N_s assuming that the remaining background comes from the $e^+e^- \rightarrow e^+e^-\eta\pi^0$ process. The obtained numbers of signal and background events are listed in Table I. The background includes both the $e^+e^- \rightarrow e^+e^-\eta\pi^0$ and $e^+e^- \rightarrow e^+e^-\eta'$ contributions. The systematic errors quoted for N_s are mainly due to the uncertainties on R_s and R_b .

VI. DETECTION EFFICIENCY

The detection efficiency is determined from MC simulation as the ratio of the true Q^2 distributions computed after and before applying the selection criteria. The Q^2 dependencies of the detection efficiencies for both processes under study are shown in Fig. 11. The detector acceptance limits the detection efficiency at small Q^2 . The cross sections are measured in the regions $Q^2 > 4 \text{ GeV}^2$, where the detection efficiencies are greater than 5%. The asymmetry of the e^+e^- collisions at PEP-II leads to different efficiencies for events with electron and positron tags. The Q^2 range from 4 to 6 GeV^2 is measured only with the positron tag.

We study possible sources of systematic uncertainty due to differences between data and MC simulation in detector response. The MC simulation predicts about a 2.5% loss of signal events, weakly dependent on Q^2 , due to the offline trigger, i.e. program filters, which provide background suppression before the full event reconstruction. Events of the process under study satisfying our selection criteria pass a filter selecting events with at least three tracks in the drift chamber originating from the interaction region. The filter inefficiency is measured from data using a small fraction of selected events that does not pass the background filters. Combining events from the η and η' samples, we determine the ratio of the inefficiencies in data and MC simulation to be 1.15 ± 0.20 . The error of the ratio is used to estimate the systematic uncertainty for the filter inefficiency: $0.2 \times 2.5 = 0.5\%$. The trigger inefficiency obtained using MC simulation is about 1% in the first Q^2 interval (4–5 GeV^2) and falls to zero at $Q^2 > 14 \text{ GeV}^2$. The limited statistics do not allow us to measure this inefficiency in data. Therefore, the level of the inefficiency observed in the MC simulation is taken as an estimate of the systematic uncertainty due to the trigger inefficiency.

The systematic uncertainty due to a possible difference between data and simulation in the charged-particle track reconstruction for pions is estimated to be about 0.35% per track, so the total uncertainty is 0.7%. For electron tracks, this uncertainty is about 0.1%.

The data-MC simulation difference in the pion identification efficiency is estimated using the identification efficiencies measured for pions in the $D^{*+} \rightarrow D^0\pi^+$, $D^0 \rightarrow \pi^+K^-$ decay. The ratio of the data and MC identification efficiencies is determined as a function of the pion momentum and polar angle. These functions for positive and negative pions are then convolved with the pion energy

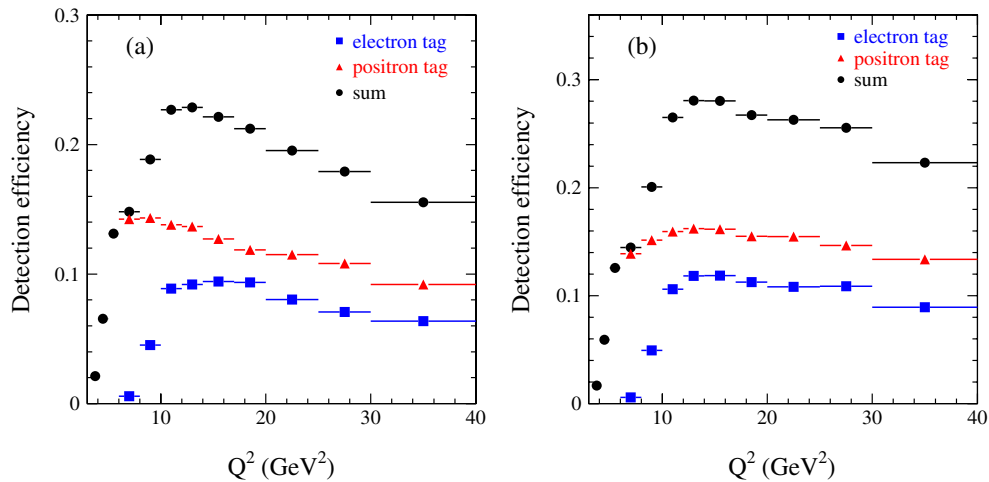


FIG. 11 (color online). The detection efficiencies for (a) $e^+e^- \rightarrow e^+e^-\eta$ with $\eta \rightarrow \pi^+\pi^-\pi^0$ and $\pi^0 \rightarrow 2\gamma$ and (b) $e^+e^- \rightarrow e^+e^-\eta'$ with $\eta \rightarrow \pi^+\pi^-\eta$ and $\eta \rightarrow 2\gamma$ as functions of the momentum transfer squared for events with a tagged electron (squares), a tagged positron (triangles), and their sum (circles). In the region $Q^2 < 6 \text{ GeV}^2$, where the electron-tag efficiency is close to zero, the sum and the positron-tag efficiencies coincide.

and angular distributions for simulated signal events in each Q^2 interval. The resulting efficiency correction (δ_π) for pion identification varies from -1% to 0.5% in the Q^2 range from 4 to 40 GeV^2 . The systematic uncertainty in the correction does not exceed 0.5% . The data-MC simulation difference in electron identification is estimated using the identification efficiencies measured for electrons in radiative Bhabha events. The found efficiency correction (δ_e) does not exceed 1% . Its systematic uncertainty is estimated to be 0.5% .

The π^0 reconstruction efficiency is studied using events from the ISR process $e^+e^- \rightarrow \gamma\omega$, $\omega \rightarrow \pi^+\pi^-\pi^0$. These events can be reconstructed and selected without using information related to the π^0 . The π^0 reconstruction efficiency is computed as the ratio of the number of events with an identified π^0 to the total number of reconstructed $e^+e^- \rightarrow \gamma\omega$ events. The data-MC simulation relative difference in the π^0 efficiency depends on the π^0 momentum and varies from $(0.7 \pm 1.2)\%$ at momenta below $0.25 \text{ GeV}/c$ to $(-4.2 \pm 1.3)\%$ at $4 \text{ GeV}/c$ [1]. The efficiency correction averaged over the π^0 spectrum is shown in Fig. 12 as a function of Q^2 . The systematic uncertainty associated with this correction is estimated to be 1% . For $\eta \rightarrow \gamma\gamma$ decays the efficiency correction is expected to be smaller. The maximum value of the π^0 efficiency correction (2%) is conservatively taken as an estimate of systematic uncertainty due to a possible data-MC simulation difference in the $\eta \rightarrow \gamma\gamma$ reconstruction.

To estimate the effect of the requirement $-0.025 < r < 0.05$, η' events with $0.05 < r < 0.075$ are studied. We calculate the double ratio minus unity

$$\frac{\Delta\sigma}{\sigma} = \frac{(N_{\text{new}}/N)_{\text{data}}}{(N_{\text{new}}/N)_{\text{MC}}} - 1, \quad (11)$$

where N_{new} and N are the numbers of signal events with the new and standard selection criteria. The ratio is sensitive to the relative change in the measured cross section due to the changes in the selection criteria. We do not observe any significant Q^2 dependence of $\Delta\sigma/\sigma$. The average over Q^2

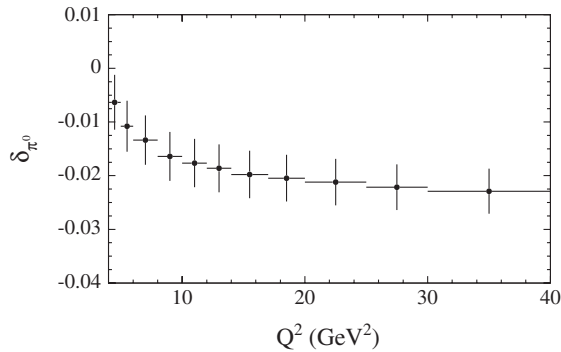


FIG. 12. The correction to the MC-estimated π^0 reconstruction efficiency δ_{π^0} as a function of Q^2 for the $e^+e^- \rightarrow e^+e^-\eta$ process.

is found to be consistent with zero (-0.003 ± 0.004). We conclude that the simulation reproduces the shape of the r distribution.

We also study the effect of the $|\cos\theta_{e\eta^{(\prime)}}^*| > 0.99$ restriction by changing the value to 0.95. The corresponding change of the measured cross section does not depend on Q^2 . The average change in cross section integrating over Q^2 is $(2.0 \pm 0.4)\%$. We consider this data-MC simulation difference (2%) as a measure of the systematic uncertainty due to the $\cos\theta_{e\eta^{(\prime)}}^*$ criterion.

The angular and energy distributions of detected particles are very different for events with electron and positron tags. As a cross-check of our study of the efficiency corrections, we have performed comparison of Q^2 dependencies of the cross sections obtained with only electron and only positron tags. For $Q^2 > 8 \text{ GeV}^2$, where both positron and electron data are available, the ratio of the cross sections have been found to be consistent with unity, for both η and η' events. The Q^2 dependence of the ratio for η events is shown in Fig. 13. Because of limited statistics, data of the three highest Q^2 bins are combined.

The main sources of systematic uncertainty associated with the detection efficiency are summarized in Table III for both processes under study. The values of the detection efficiency and the total efficiency correction $\delta_{\text{total}} = \delta_\pi + \delta_e + \delta_{\pi^0}$ (the term δ_{π^0} is only applicable to the η mode) for different Q^2 intervals are listed in Tables I and II. The data distribution is corrected as follows:

$$N_i^{\text{corr}} = N_i / (1 + \delta_{\text{total},i}), \quad (12)$$

where N_i is the number of signal events in the i th Q^2 interval.

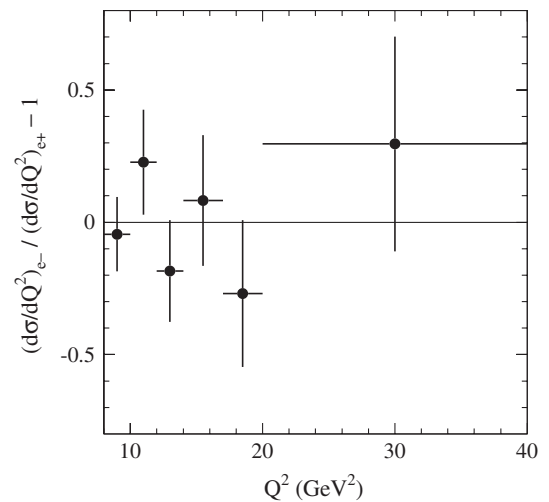


FIG. 13. The ratio of the cross sections for the $e^+e^- \rightarrow e^+e^-\eta$ process measured with electron and positron tags as a function of Q^2 .

TABLE III. The main sources of systematic uncertainty associated with the detection efficiency, and the total efficiency systematic uncertainty for $e^+e^- \rightarrow e^+e^-\eta$ and $e^+e^- \rightarrow e^+e^-\eta'$ events.

Source	η (%)	η' (%)
Track reconstruction		0.8
π^\pm identification		0.5
e^\pm identification		0.5
$ \cos\theta_{e\eta^{(\prime)}}^* > 0.99$ criterion		2.0
Trigger, filters	0.7	1.3
$\eta, \pi^0 \rightarrow 2\gamma$ reconstruction	1.0	2.0
Total	2.6	3.3

VII. CROSS SECTION AND FORM FACTOR

The Born differential cross section for $e^+e^- \rightarrow e^+e^-\eta^{(\prime)}$ is

$$\frac{d\sigma}{dQ^2} = \frac{(dN/dQ^2)_{\text{corr}}^{\text{unfolded}}}{\varepsilon RLB} \quad (13)$$

where $(dN/dQ^2)_{\text{corr}}^{\text{unfolded}}$ is the mass spectrum corrected for data-MC simulation differences and unfolded for detector resolution effects as explained below, L is the total integrated luminosity, ε is the Q^2 -dependent detection efficiency, and R is a radiative correction factor accounting for distortion of the Q^2 spectrum due to vacuum polarization effects and the emission of soft photons from the initial-state particles. The factor B is the product of the branching fractions, $\mathcal{B}(\eta \rightarrow \pi^+\pi^-\pi^0)\mathcal{B}(\pi^0 \rightarrow \gamma\gamma) = 0.2246 \pm 0.0028$ or $\mathcal{B}(\eta' \rightarrow \pi^+\pi^-\eta)\mathcal{B}(\eta \rightarrow \gamma\gamma) = 0.1753 \pm 0.0056$ [16].

The radiative correction factor R is determined using simulation at the generator level, i.e., without detector simulation. The Q^2 spectrum is generated using only the pure Born amplitude for the $e^+e^- \rightarrow e^+e^-\eta^{(\prime)}$ process,

and then using a model with radiative corrections included. The radiative correction factor, evaluated as the ratio of the second spectrum to the first, varies from 0.994 at $Q^2 = 4 \text{ GeV}^2$ to 1.002 at $Q^2 = 40 \text{ GeV}^2$. The accuracy of the radiative correction calculation is estimated to be 1% [13]. It should be noted that the value of R depends on the requirement on the extra photon energy. The Q^2 dependence obtained corresponds to the condition $r = 2E_\gamma^*/\sqrt{s} < 0.1$ imposed in the simulation.

The corrected and unfolded Q^2 distribution $(dN/dQ^2)_{\text{corr}}^{\text{unfolded}}$ is obtained from the measured distribution by dividing by the efficiency correction factor (see Eq. (12)) and unfolding for the effect of finite Q^2 resolution. Using MC simulation, a migration matrix H is obtained, which represents the probability that an event with true Q^2 in interval j is reconstructed in interval i :

$$\left(\frac{dN}{dQ^2}\right)_i^{\text{rec}} = \sum_j H_{ij} \left(\frac{dN}{dQ^2}\right)_j^{\text{true}}. \quad (14)$$

In the case of extra photon emission, Q_{true}^2 is calculated as $-(p-p'-k)^2$, where k is the photon four-momentum; ε and R in Eq. (13) are functions of Q_{true}^2 . As the chosen Q^2 interval width significantly exceeds the resolution for all Q^2 , nonzero elements of the migration matrix lie on and near the diagonal. The values of the diagonal elements are in the range 0.9–0.95. The true Q^2 distribution is obtained by applying the inverse of the migration matrix to the measured distribution. The procedure does not change the shape of the Q^2 distribution significantly, but increases the errors (by about 10%) and their correlations. The number of events ($N_{\text{corr}}^{\text{unfolded}}$) as a function of Q^2 is reported in Tables I and II.

The value of the differential cross section as a function of Q^2 is listed in Tables IV and V. The quoted errors are statistical and systematic. The latter includes only

TABLE IV. The Q^2 interval, the weighted average Q^2 value for the interval (\bar{Q}^2), the $e^+e^- \rightarrow e^+e^-\eta$ cross section ($d\sigma/dQ^2(\bar{Q}^2)$), and the product of the $\gamma\gamma^* \rightarrow \eta$ transition form factor $F(\bar{Q}^2)$ and \bar{Q}^2 . The statistical and systematic errors are quoted separately for the cross sections, and are combined for the form factors. In the table, we quote the Q^2 -dependent systematic errors. The Q^2 -independent error is 3.5% for the cross section and 2.9% for the form factor.

Q^2 interval (GeV ²)	\bar{Q}^2 (GeV ²)	$d\sigma/dQ^2(\bar{Q}^2)$ (fb/GeV ²)	$\bar{Q}^2 F(\bar{Q}^2) $ (MeV)
4–5	4.47	$95.6 \pm 5.1 \pm 3.1$	143.4 ± 4.4
5–6	5.47	$46.6 \pm 2.7 \pm 1.7$	142.7 ± 4.9
6–8	6.89	$20.4 \pm 1.2 \pm 0.8$	142.6 ± 5.2
8–10	8.92	$9.06 \pm 0.72 \pm 0.35$	151.2 ± 6.7
10–12	10.96	$4.67 \pm 0.47 \pm 0.18$	158.5 ± 8.5
12–14	12.92	$2.16 \pm 0.34 \pm 0.10$	146.5 ± 12.1
14–17	15.38	$1.65 \pm 0.22 \pm 0.06$	178.9 ± 12.1
17–20	18.34	$0.61 \pm 0.14 \pm 0.02$	151.6 ± 17.8
20–25	22.33	$0.33 \pm 0.08 \pm 0.01$	166.0 ± 20.2
25–30	27.23	$0.15 \pm 0.06 \pm 0.01$	166.7 ± 36.6
30–40	34.38	$0.085 \pm 0.032 \pm 0.003$	205.9 ± 39.0

TABLE V. The Q^2 interval, the weighted average Q^2 value for the interval (\bar{Q}^2), the $e^+e^- \rightarrow e^+e^-\eta'$ cross section ($d\sigma/dQ^2(\bar{Q}^2)$), and the product of the $\gamma\gamma^* \rightarrow \eta'$ transition form factor $F(\bar{Q}^2)$ and \bar{Q}^2 . The statistical and systematic errors are quoted separately for the cross sections, and are combined for the form factors. In the table we quote the Q^2 -dependent systematic errors. The Q^2 -independent error is 5.3% for the cross section and 3.5% for the form factor.

Q^2 interval (GeV ²)	\bar{Q}^2 (GeV ²)	$d\sigma/dQ^2(\bar{Q}^2)$ (fb/GeV ²)	$\bar{Q}^2 F(\bar{Q}^2) $ (MeV)
4–5	4.48	$202 \pm 7 \pm 3$	216.2 ± 4.3
5–6	5.46	$99.6 \pm 3.6 \pm 1.4$	214.3 ± 4.1
6–8	6.90	$51.7 \pm 1.6 \pm 0.5$	233.3 ± 3.9
8–10	8.92	$22.1 \pm 0.9 \pm 0.2$	241.6 ± 5.2
10–12	10.95	$10.8 \pm 0.6 \pm 0.1$	245.5 ± 6.7
12–14	12.90	$5.45 \pm 0.41 \pm 0.06$	236.7 ± 8.9
14–17	15.33	$3.10 \pm 0.24 \pm 0.04$	248.5 ± 9.9
17–20	18.33	$1.70 \pm 0.18 \pm 0.02$	258.7 ± 13.7
20–25	22.36	$0.77 \pm 0.09 \pm 0.01$	257.0 ± 15.4
25–30	27.20	$0.30 \pm 0.06 \pm 0.01$	240.0 ± 25.7
30–40	34.32	$0.098 \pm 0.031 \pm 0.002$	224.1 ± 35.9

Q^2 -dependent errors: the systematic uncertainty in the number of signal events and the statistical errors on the efficiency correction and MC simulation. The Q^2 -independent systematic error on the $e^+e^- \rightarrow e^+e^-\eta$ cross section is 3.5%; this results from the uncertainties on the detection efficiency, both systematic (2.6%) and model-dependent (1.5%), the uncertainty in the calculation of the radiative correction factor (1%), and the errors on the integrated luminosity (1%) and the η decay branching fraction (1.2%) [16]. The Q^2 -independent systematic error on the $e^+e^- \rightarrow e^+e^-\eta'$ cross section is 5.3%. It includes the systematic and model uncertainties on the detection efficiency (3.3% and 1.5%, respectively), the uncertainties on the background subtraction (1.6%) and the radiative correction factor (1%), and the errors on the integrated luminosity (1%) and the η' decay branching fraction (3.2%) [16].

The model dependence of the detection efficiency arises from the unknown cross-section dependence on the momentum transfer to the untagged electron. The MC simulation is performed, and the detection efficiency is determined, with the restriction that the momentum transfer to the untagged electron be greater than -0.6 GeV², so that the cross section is measured for the restricted range $|q_2^2| < 0.6$ GeV². The actual q_2^2 threshold is determined by the requirement on $\cos\theta_{e\eta^{(l)}}^*$ and is equal to 0.38 GeV². The MC simulation is performed with a q_2^2 independent form factor, which corresponds to the QCD-inspired model $F(q_1^2, q_2^2) \propto 1/(q_1^2 + q_2^2) \approx 1/q_1^2$ [17]. The event loss due to the $|q_2^2| < 0.38$ GeV² restriction is about 2.5%. The use of the form factor predicted by the vector dominance model $F(q_2^2) \propto 1/(1 - q_2^2/m_\rho^2)$, where m_ρ is ρ meson mass, leads to a decreased event loss of only 1%. The difference between these efficiencies is considered to be an estimate of the model uncertainty due to the unknown q_2^2 dependence.

Because of the strong nonlinear dependence of the cross section on Q^2 , the effective value of Q^2 corresponding to the measured cross section differs from the center of the Q^2 interval. We parametrize the measured cross section with a smooth function and calculate \bar{Q}^2 for each Q^2 interval solving the equation

$$d\sigma/d(Q^2)(\bar{Q}^2) = d\sigma/d(Q^2)_{\text{average}},$$

where $d\sigma/d(Q^2)_{\text{average}}$ is the differential cross section averaged over the interval. The values of \bar{Q}^2 are listed in Table IV and V. The measured differential cross sections for both processes under study are shown in Fig. 14, together with the data reported by the CLEO Collaboration [9] for $Q^2 > 3.5$ GeV². We average the CLEO results obtained in different $\eta^{(l)}$ decay modes assuming that systematic errors for different modes are not correlated.

To extract the transition form factor, the measured and calculated cross sections are compared. The simulation uses a constant form factor F_{MC}^2 . Therefore, the measured form factor is determined from

$$|F(Q^2)|^2 = \frac{(d\sigma/dQ^2)_{\text{data}}}{(d\sigma/dQ^2)_{\text{MC}}} F_{\text{MC}}^2. \quad (15)$$

The calculated cross section $(d\sigma/dQ^2)_{\text{MC}}$ has a model-dependent uncertainty due to the unknown dependence on the momentum transfer to the untagged electron. The difference between the cross section values calculated with the two form-factor models described above is 4.6% for both η and η' . This difference is considered to be an estimate of the model uncertainty due to the unknown q_2^2 dependence. The values of the form factors obtained, represented in the form $\bar{Q}^2|F(\bar{Q}^2)|$, are listed in Tables IV and V and shown in Fig. 15. For the form factor, we quote the combined error, obtained by adding the statistical and Q^2 -dependent systematic uncertainties in quadrature. The

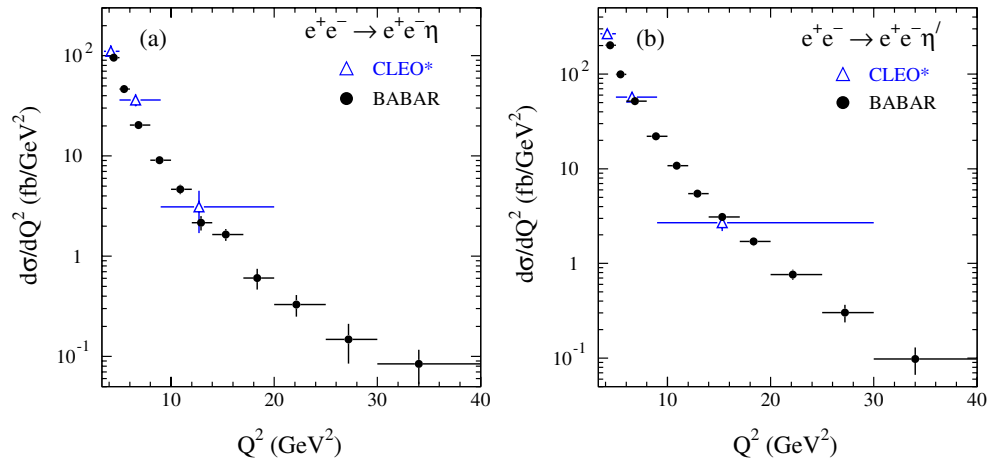


FIG. 14 (color online). The differential cross sections for (a) $e^+e^- \rightarrow e^+e^-\eta$ and (b) $e^+e^- \rightarrow e^+e^-\eta'$ from the present analysis compared to those from the CLEO experiment [9]. The asterisk near the label ‘‘CLEO’’ in this and the next figures indicates that the original CLEO results obtained in different $\eta^{(\prime)}$ decay modes were averaged assuming that systematic errors for different modes are not correlated. In the present analysis the cross sections are measured with the restriction $|q_2^2| < 0.6 \text{ GeV}^2$. In the CLEO analysis, the cross sections have been obtained using the vector dominance model for the q_2^2 dependence in simulation.

Q^2 -independent systematic error is 2.9% for the η and 3.5% for the η' form factor.

VIII. DISCUSSION AND SUMMARY

The comparison of our results on the form factors with the most precise previous measurements [9] is shown in Fig. 15. For the η' form factor, our results are in good agreement with those reported by the CLEO Collaboration [9]. For the η form factor the agreement is worse. In particular, the CLEO point at $Q^2 \approx 7 \text{ GeV}^2$ lies higher than our measurements by about 3 standard deviations.

The data for the $e^+e^- \rightarrow \eta^{(\prime)}\gamma$ reactions are used to determine the transition form factors in the timelike region $q^2 = s > 0$. Since the time- and spacelike form factors are expected to be similar at high Q^2 , in Fig. 16 we show the results of the high- Q^2 timelike measurements together with the spacelike data. The form factors at $Q^2 = 14.2 \text{ GeV}^2$ are obtained from the values of the $e^+e^- \rightarrow \eta^{(\prime)}\gamma$ cross

sections measured by CLEO [18] near the peak of the $\psi(3770)$ resonance. We calculate the form factor using the formulas from Ref. [19] under the assumption that the contributions of the $\psi(3770) \rightarrow \eta^{(\prime)}\gamma$ decays to the $e^+e^- \rightarrow \eta^{(\prime)}\gamma$ cross sections are negligible. It is seen that the measured time- and spacelike form factors at $Q^2 \approx 14 \text{ GeV}^2$ are in agreement both for η and for η' . The BABAR measurements of the $e^+e^- \rightarrow \eta^{(\prime)}\gamma$ cross sections [19] allow us to extend the Q^2 region for the η and η' form factor measurements up to 112 GeV^2 .

In most models for the meson distribution amplitude $\phi_P(x)$ used for calculation of photon-meson transition form factors, the DA end-point behavior is determined by the factor $x(1-x)$. The form factors calculated with such conventional DAs are almost flat for Q^2 values greater than 15 GeV^2 (see, for example, the recent works [20–22] devoted to the $\gamma\gamma^* \rightarrow \pi^0$ form-factor). Some of these models [20] have difficulties in reproducing the

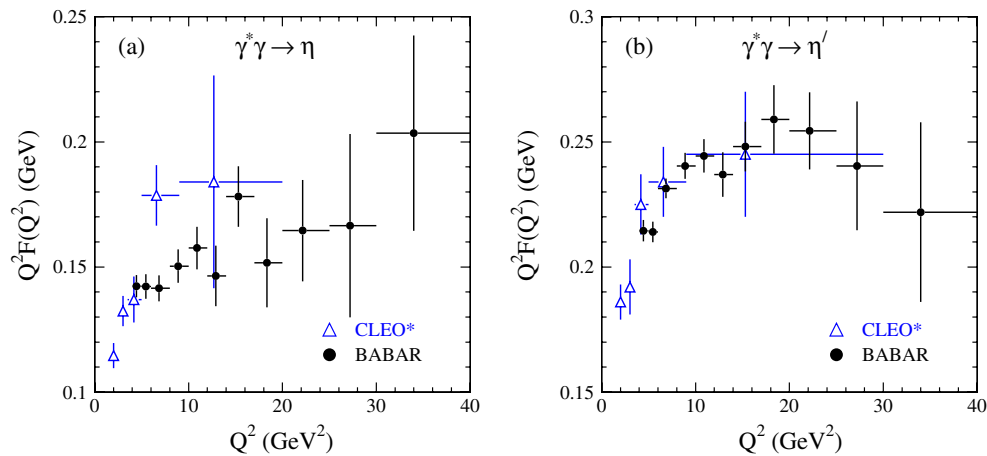


FIG. 15 (color online). The transition form factors multiplied by Q^2 for (a) $\gamma\gamma^* \rightarrow \eta$ and (b) $\gamma\gamma^* \rightarrow \eta'$.

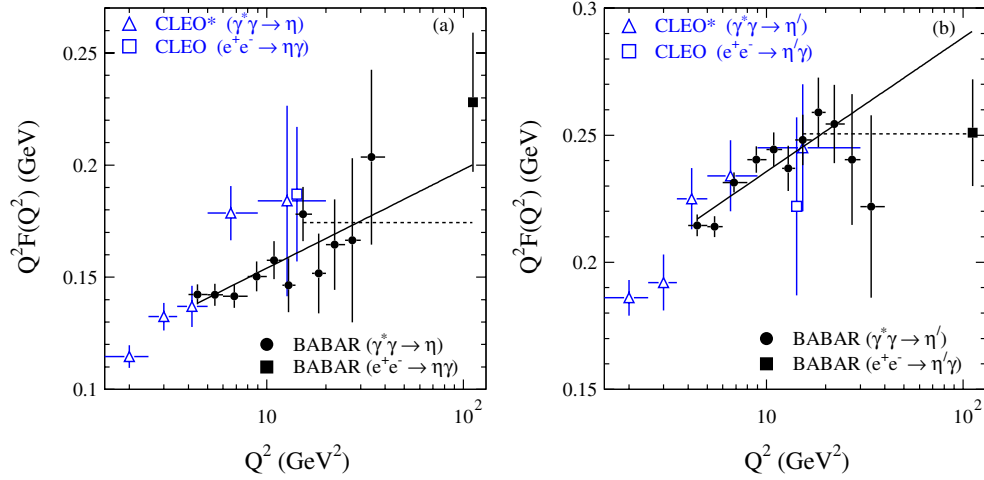


FIG. 16 (color online). The transition form factors multiplied by Q^2 for (a) $\gamma\gamma^* \rightarrow \eta$ and (b) $\gamma\gamma^* \rightarrow \eta'$. The solid line shows the result of the fit to *BABAR* data by the function given by Eq. (16). The dashed lines indicate the average form factor values over the data points with $Q^2 > 14 \text{ GeV}^2$.

Q^2 dependence of the $\gamma\gamma^* \rightarrow \pi^0$ form-factor measured by *BABAR* [1] in the Q^2 range from 4 to 40 GeV^2 . Alternatively, models with a flat DA or a DA that is finite at the end points have been suggested [23–25], which give a logarithmic rise of the product $Q^2 F(Q^2)$ with Q^2 and describe the *BABAR* data reasonably well.

The Q^2 dependencies of the products $Q^2 F(Q^2)$ for η and η' are fit with the function

$$Q^2 F(Q^2) = b_l + a_l \ln Q^2 (\text{GeV}^2). \quad (16)$$

The results of the fit are shown in Fig. 16. For both η and η' , the quality of the fit is acceptable: χ^2/ν is equal to 6.8/10 for η and 15.9/10 for η' , where ν is the number of degrees of freedom. The observed rise of the form factors ($a_l \approx 0.20 \pm 0.05 \text{ GeV}$) is about three times weaker than the corresponding rise of the π^0 form factor [24].

The dashed horizontal lines in Fig. 16 show the results of fits assuming $Q^2 F(Q^2)$ to be constant for $14 < Q^2 < 112 \text{ GeV}^2$. The average values of $Q^2 F(Q^2)$ in this range are $0.175 \pm 0.008 \text{ GeV}$ for η and $0.251 \pm 0.006 \text{ GeV}$ for η' . The χ^2/ν for the fits are 5.6/5 for the η and 1.3/5 for the η' . The preferred description for the η form factor is the logarithmic function of Eq. (16), corresponding to the models with a finite DA at the end points. The η' form factor is better described by the model with a conventional DA, yielding a flat $Q^2 F(Q^2)$ for $Q^2 > 15 \text{ GeV}^2$.

To compare the measured values of the η and η' form factors with theoretical predictions and data for the π^0 form factor, we use the description of η - η' mixing in the quark flavor basis [26]:

$$\begin{aligned} |n\rangle &= \frac{1}{\sqrt{2}}(|\bar{u}u\rangle + |\bar{d}d\rangle), & |s\rangle &= |\bar{s}s\rangle, \\ |\eta\rangle &= \cos\phi|n\rangle - \sin\phi|s\rangle, & |\eta'\rangle &= \sin\phi|n\rangle + \cos\phi|s\rangle, \end{aligned} \quad (17)$$

where ϕ is the mixing angle. The η and η' transition form factors are related to the form factors for the $|n\rangle$ and $|s\rangle$ states:

$$F_\eta = \cos\phi F_n - \sin\phi F_s, \quad F_{\eta'} = \sin\phi F_n + \cos\phi F_s, \quad (18)$$

which have asymptotic limits for $Q^2 \rightarrow \infty$ [27] given by

$$Q^2 F_s(Q^2) = \frac{2}{3} f_s, \quad Q^2 F_n(Q^2) = \frac{5\sqrt{2}}{3} f_n, \quad (19)$$

where f_n and f_s are the decay constants for the $|n\rangle$ and $|s\rangle$ states, respectively. For the π^0 form factor, the corresponding asymptotic value is $\sqrt{2}f_\pi$. The pion decay constant is determined from leptonic π decays to be $130.4 \pm 0.2 \text{ MeV}$ [16]. For the $|n\rangle$ and $|s\rangle$ states, we use the “theoretical” values from Ref. [26]: $f_n = f_\pi$ and $f_s = \sqrt{2f_K^2 - f_\pi^2} \approx 1.36f_\pi$ ($f_K/f_\pi = 1.193 \pm 0.006$ [16]), which agree to within 10% with the “phenomenological” values [26] extracted from the analysis of experimental data, for example, for the two-photon η and η' decays. The currently accepted value of the mixing angle ϕ is about 41° [28]. Under the assumption that the $|n\rangle$ and π^0 distribution amplitudes are similar to each other, the only difference between the $|n\rangle$ and π^0 form factors is a factor of 3/5 that arises from the quark charges. In Fig. 17, the form factor for the $|n\rangle$ -state multiplied by $3Q^2/5$ is compared with the measured $\gamma^*\gamma \rightarrow \pi^0$ form factor [1] and the results of the QCD calculations performed by A.P. Bakulev, S.V. Mikhailov and N.G. Stefanis [29] for the asymptotic DA [30], the Chernyak-Zhitnitsky π^0 DA [31], and the π^0 DA derived from QCD sum rules with nonlocal condensates [32]. The horizontal dashed line indicates the asymptotic limit for the π^0 form factor.

The Q^2 dependencies of the measured $|n\rangle$ and π^0 form factors are significantly different. This indicates that the distribution amplitudes for the $|n\rangle$ and π^0 are significantly different as well. The data for the $|n\rangle$ form factor are well

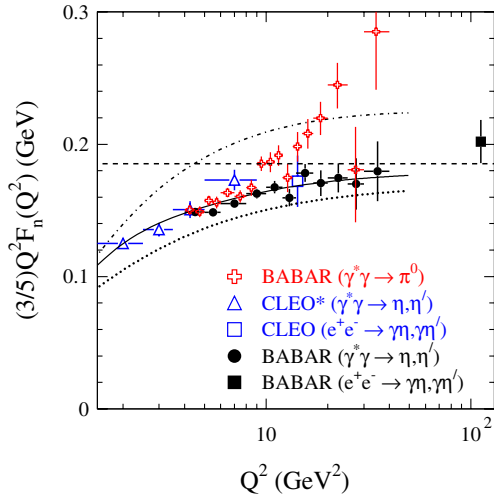


FIG. 17 (color online). The $\gamma\gamma^* \rightarrow |n\rangle$ transition form factor multiplied by $3Q^2/5$ in comparison with the $\gamma\gamma^* \rightarrow \pi^0$ transition form factor [1]. The dashed line indicates the asymptotic limit for the π^0 form factor. The dotted, dash-dotted, and solid curves show predictions of Ref. [29] for the asymptotic DA [30], the Chernyak-Zhitnitsky π^0 DA [31], and the π^0 DA from Ref. [32], respectively.

described by the model with DA from Ref. [32], while the data for the π^0 form factor is reproduced by the models with a significantly wider DA [21,22] or a flat DA [23–25].

The form factor for the $|s\rangle$ state is shown in Fig. 18. The dotted curve shows the QCD prediction [29] for the asymptotic DA [30], defined by multiplying the π^0 curve in Fig. 17 by a factor of $(\sqrt{2}/3)f_s/f_\pi$. The data lie systematically below this prediction. This may indicate, in particular, that the distribution amplitude for the $|s\rangle$ state is narrower than the asymptotic DA. However, due to the strong sensitivity of the result for the $|s\rangle$ state to mixing parameters, other interpretations are possible. For example, an admixture of the two-gluon component in the η' meson [33–36] can lead to a significant shift of the values of the $|s\rangle$ form factor.

In summary, we have studied the $e^+e^- \rightarrow e^+e^-\eta$ and $e^+e^- \rightarrow e^+e^-\eta'$ reactions and measured the differential cross sections ($d\sigma/dQ^2$) and the $\gamma^*\gamma \rightarrow \eta^{(\prime)}$ transition form factors $F(Q^2)$ in the momentum transfer range from 4 to 40 GeV^2 . In general, our results are in reasonable agreement with the previous CLEO measurements [9]. We significantly improve the precision and extend the Q^2 region for form factor measurements.

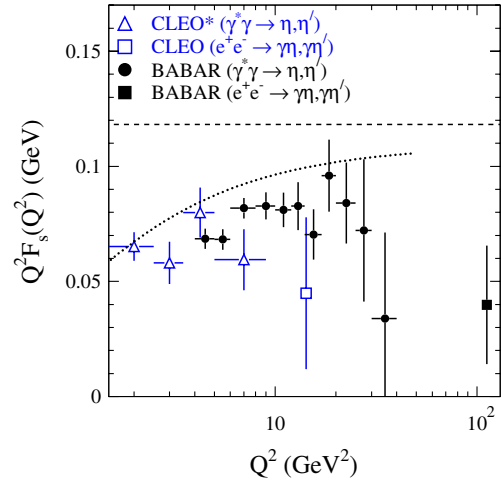


FIG. 18 (color online). The $\gamma\gamma^* \rightarrow |s\rangle$ transition form factor multiplied by Q^2 . The dashed line indicates the asymptotic limit for the form factor. The dotted curve shows the prediction [29] for the asymptotic DA [30].

ACKNOWLEDGMENTS

We thank V. L. Chernyak for useful discussions. We are grateful for the extraordinary contributions of our PEP-II colleagues in achieving the excellent luminosity and machine conditions that have made this work possible. The success of this project also relies critically on the expertise and dedication of the computing organizations that support *BABAR*. The collaborating institutions wish to thank SLAC for its support and the kind hospitality extended to them. This work is supported by the U.S. Department of Energy and National Science Foundation, the Natural Sciences and Engineering Research Council (Canada), the Commissariat à l'Énergie Atomique and Institut National de Physique Nucléaire et de Physique des Particules (France), the Bundesministerium für Bildung und Forschung and Deutsche Forschungsgemeinschaft (Germany), the Istituto Nazionale di Fisica Nucleare (Italy), the Foundation for Fundamental Research on Matter (The Netherlands), the Research Council of Norway, the Ministry of Education and Science of the Russian Federation, Ministerio de Ciencia e Innovación (Spain), and the Science and Technology Facilities Council (United Kingdom). Individuals have received support from the Marie-Curie IEF program (European Union), the A. P. Sloan Foundation (USA) and the Binational Science Foundation (USA-Israel).

- [1] B. Aubert *et al.* (*BABAR* Collaboration), *Phys. Rev. D* **80**, 052002 (2009).
 [2] J. P. Lees *et al.* (*BABAR* Collaboration), *Phys. Rev. D* **81**, 052010 (2010).

- [3] S. J. Brodsky, T. Kinoshita, and H. Terazawa, *Phys. Rev. D* **4**, 1532 (1971).
 [4] G. P. Lepage and S. J. Brodsky, *Phys. Rev. D* **22**, 2157 (1980).

- [5] C. Berger *et al.* (PLUTO Collaboration), *Phys. Lett. B* **142**, 125 (1984).
- [6] H. Aihara *et al.* (TPC/Two Gamma Collaboration), *Phys. Rev. Lett.* **64**, 172 (1990).
- [7] H.J. Behrend *et al.* (CELLO Collaboration), *Z. Phys. C* **49**, 401 (1991).
- [8] M. Acciarri *et al.* (L3 Collaboration), *Phys. Lett. B* **418**, 399 (1998).
- [9] J. Gronberg *et al.* (CLEO Collaboration), *Phys. Rev. D* **57**, 33 (1998).
- [10] B. Aubert *et al.* (BABAR Collaboration), *Nucl. Instrum. Methods Phys. Res., Sect. A* **479**, 1 (2002).
- [11] V.P. Druzhinin, L.A. Kardapoltsev, and V.A. Tayursky, [arXiv:1010.5969](https://arxiv.org/abs/1010.5969).
- [12] V.M. Budnev, I.F. Ginzburg, G.V. Meledin, and V.G. Serbo, *Phys. Rep.* **15**, 181 (1975).
- [13] S. Ong and P. Kessler, *Phys. Rev. D* **38**, 2280 (1988).
- [14] S. Agostinelli *et al.* (GEANT4 Collaboration), *Nucl. Instrum. Methods Phys. Res., Sect. A* **506**, 250 (2003).
- [15] D. Antreasyan *et al.* (Crystal Ball Collaboration), *Phys. Rev. D* **33**, 1847 (1986); S. Uehara *et al.* (Belle Collaboration), *Phys. Rev. D* **80**, 032001 (2009).
- [16] K. Nakamura *et al.* (Particle Data Group), *J. Phys. G* **37**, 075021 (2010).
- [17] G. Kopp, T.F. Walsh, and P.M. Zerwas, *Nucl. Phys.* **B70**, 461 (1974).
- [18] T.K. Pedlar *et al.* (CLEO Collaboration), *Phys. Rev. D* **79**, 111101 (2009).
- [19] B. Aubert *et al.* (BABAR Collaboration), *Phys. Rev. D* **74**, 012002 (2006).
- [20] S. V. Mikhailov and N. G. Stefanis, *Nucl. Phys.* **B821**, 291 (2009).
- [21] A. Khodjamirian, *Int. J. Mod. Phys. A* **25**, 513 (2010).
- [22] V.L. Chernyak, [arXiv:0912.0623](https://arxiv.org/abs/0912.0623).
- [23] A. E. Dorokhov, *Phys. Part. Nucl. Lett.* **7**, 229 (2010).
- [24] A. V. Radyushkin, *Phys. Rev. D* **80**, 094009 (2009).
- [25] M. V. Polyakov, *JETP Lett.* **90**, 228 (2009).
- [26] T. Feldmann, P. Kroll, and B. Stech, *Phys. Rev. D* **58**, 114006 (1998).
- [27] T. Feldmann and P. Kroll, *Phys. Rev. D* **58**, 057501 (1998).
- [28] C.E. Thomas, *J. High Energy Phys.* **10** (2007) 026.
- [29] A.P. Bakulev, S. V. Mikhailov, and N.G. Stefanis, *Phys. Rev. D* **67**, 074012 (2003); *Phys. Lett. B* **578**, 91 (2004).
- [30] G.P. Lepage and S.J. Brodsky, *Phys. Lett. B* **87**, 359 (1979).
- [31] V.L. Chernyak and A.R. Zhitnitsky, *Nucl. Phys.* **B201**, 492 (1982); **B214**, 547(E) (1983).
- [32] A.P. Bakulev, S. V. Mikhailov, and N.G. Stefanis, *Phys. Lett. B* **508**, 279 (2001); **590**, 309(E) (2004).
- [33] V.N. Baier and A.G. Grozin, *Nucl. Phys.* **B192**, 476 (1981).
- [34] A. Ali and A. Y. Parkhomenko, *Phys. Rev. D* **65**, 074020 (2002).
- [35] P. Kroll and K. Passek-Kumericki, *Phys. Rev. D* **67**, 054017 (2003).
- [36] S. S. Agaev and N. G. Stefanis, *Phys. Rev. D* **70**, 054020 (2004).